CHALMERS
UNIVERSITY OF TECHNOLOGY

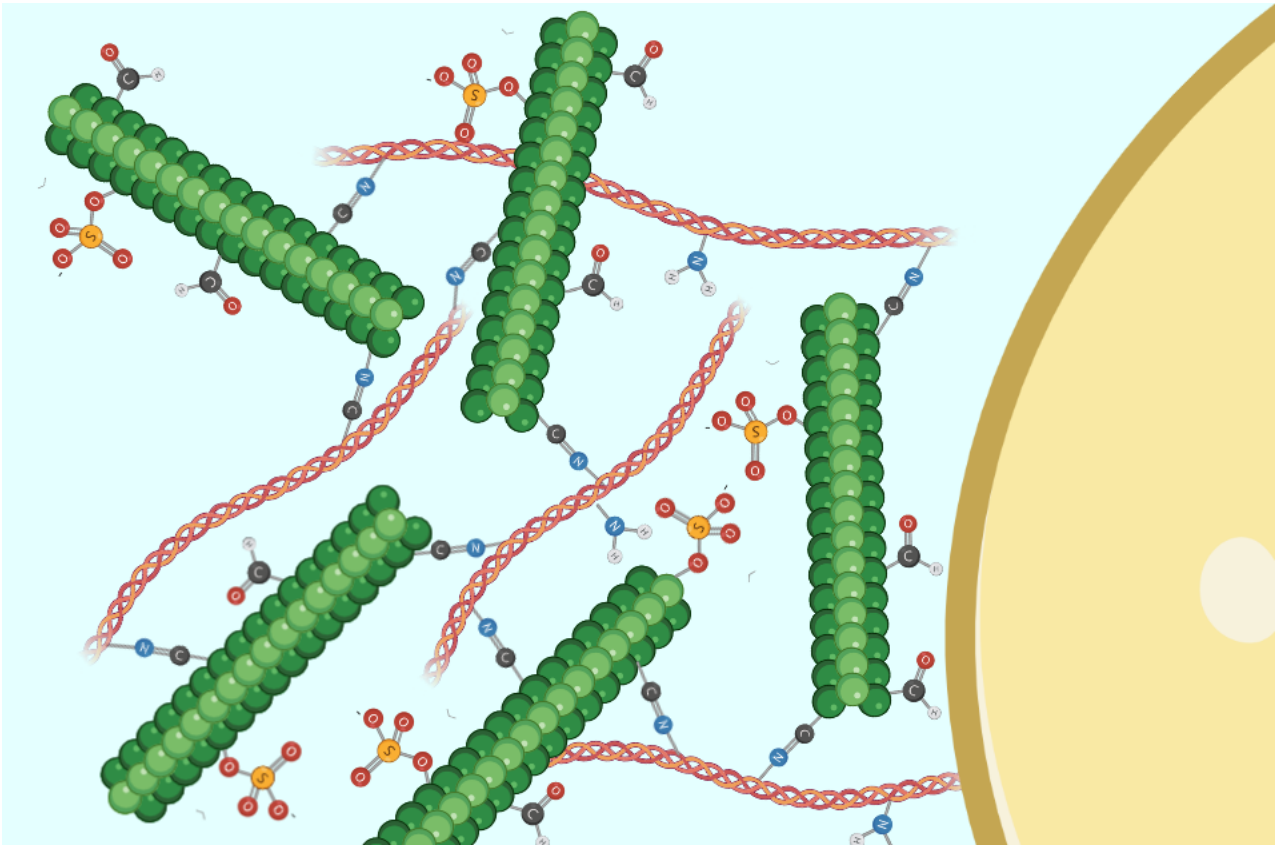

# Nanocellulose Oxidation - Fundamentals and Application in Hydrogels

SAÜL LLÀCER NAVARRO

Department of Chemistry and Chemical Engineering
Chalmers University of Technology
Göteborg, Sweden 2021

THESIS FOR THE DEGREE OF LICENCIATE OF ENGINEERING

# Nanocellulose Oxidation - Fundamentals and Application in Hydrogels

SAÜL LLÀCER NAVARRO

Department of Chemistry and Chemical Engineering
CHALMERS UNIVERSITY OF TECHNOLOGY
Göteborg, Sweden 2021

Nanocellulose Oxidation - Fundamentals and Application in Hydrogels
SAÜL LLÀCER NAVARRO



Licentiatuppsatser vid Institutionen för kemi och kemiteknik

Chalmers tekniska högskola
Nr 2021:10

Department of Chemistry and Chemical Engineering
Chalmers University of Technology
SE-412 96 Gothenburg
Telephone +46 31 772 1000

Cover:
Illustration of cellulose nanocrystal and gelatin forming a hydrogel that is capable of entrapping oil droplets. Created with BioRender.com.

Printed by Chalmers Reproservice
Gothenburg, Sweden 2021

*To my family...*

Nanocellulose Oxidation - Fundamentals and Application in Hydrogels

SAUL LLÀCER NAVARRO
Department of Chemistry and Chemical Engineering
Chalmers University of Technology

# ABSTRACT

The adaptable surface chemistry of cellulose nanocrystals (CNCs) makes them outstanding; it provides colloidal stability, which is essential for engineering use, to commercially-available CNCs. Colloidal stability is achieved by the bulky negatively-charged sulfate half-ester groups on the surface that it manufactures itself via the use of sulfuric acid. The surface chemistry of CNCs can also be adapted into dialdehyde cellulose nanocrystals (DAC) by periodate oxidation in the presence of the sulfate half-ester groups. The oxidation extends the range of applications of CNCs. The objective of this thesis is to elucidate the role played by the sulfate half-ester groups on the oxidation reaction, both in the kinetics and its products. The results demonstrate that the oxidation reaction reduces the number of sulfate half-ester groups, which impacts on the colloidal stability, the size of the resulting product properties and, consequently, the DAC applications. A rheology study and a proof-of-concept demonstration are also performed to verify whether CNC derivatives could reinforce emulsions solidified by gelatin, as this could extend the range of CNCs in the field of microwave technology to be used as a fat phantom. The gelatin emulsions reinforced by CNC derivatives maintain the storage modulus above the loss modulus at temperatures above 40 $^{o}$C. The thermal stability of the reinforced emulsions could permit the successful implementation of these gels in the field of microwave technology. CNCs are possibly the better candidate than DAC for the reinforcement due to a combination of the ease of the phantom production and performance.

Keywords: Nanocellulose, cellulose oxidation, sulfate half-ester group, polysaccharide hydrogels.

# Acknowledgements

First of all, I would like to express my gratitude to my supervisor, Tiina Nypelö, not only for giving me the opportunity to begin this scientific journey but also for teaching and inspiring me and to my co-supervisors, Anna Ström and Hana Dobšíček Trefná, for sharing so much of their knowledge in this interdisciplinary project.

Thank you, Group x3, for the pleasant environment you created and your willingness to help each other. I'd like to thank my friends and colleagues at the Division of Applied Chemistry, and my co-workers from all over Chalmers. Special thanks go to my examiner Hanna Härelind who, as Head of the Department, created such a nice place in which to work.

The Spanish/Latino mafia is thanked for making it easier for me to occupy my heart and my free time, and to keep me smiling (but not, however, for the $voluntad\ de\ gata$!). I can't forget my friends in Valencia, either: despite the distance and the fact that we cannot see or talk to each other very often, everything is like the very first day, or even better.

The financial support provided by Knut & Alice Wallenberg Foundation through the Wallenberg Wood Science Center towards my Ph.D. project is acknowledged.

Finally, my deepest gratitude go to my parents, Rosana and Jose, and my brother, Frank. Thank you for always supporting me in everything I have undertaken, including moving away from Valencia: I know how tough it has been on you.

Saül Llàcer Navarro, Göteborg, May 2021

# LIST OF PUBLICATIONS

I. Saül Llàcer Navarro, Koyuru Nakayama, Alexander Idström, Lars Evenäs, Anna Ström and Tiina Nypelö. The effect of sulfate half-ester groups on cellulose nanocrystal periodate oxidation. Submitted.

II. Hana Dobšíček Trefná, Saül Llàcer Navarro, Fredrik Lorentzon, Tiina Nypelö and Anna Ström. Fat tissue equivalent phantoms for microwave applications by reinforcing gelatin with nanocellulose. Submitted.

# AUTHOR CONTRIBUTION

I. Planned experiments with the co-authors; performed all experiments; and wrote the manuscript with the support of the co-authors. Main author.

II. Co-performed the development of the phantom formulation and analyses thereof. Co-author.

# Nomenclature

**Chemistry**

[P] Periodate concentration (mol/L)

AGU Anhydroglucose unit

CNCs Cellulose nanocrystals

CNF Cellulose nanofibrils

DAC Dialdehyde cellulose

desulfCNC Desulfated CNC

DO Degree of oxidation (%)

DSS Degree of surface substitution (%)

**Microwave technology**

QA Quality assurance

**Other**

$f$ Frequency (Hz)

$R$ Ratio

A Area

AFM Atomic force microscopy

CI Crystallinity index (%)

COD Coefficient of determination

FTIR Fourier transform infrared spectroscopy

G' Storage modulus (Pa)

G" Storage modulus (Pa)

| | |
|---|---|
| IR | Infrared |
| L | Crystallite size (nm) |
| NMR | Nuclear magnetic resonance |
| T | Temperature (°C) |
| UV | Ultraviolet |
| WAXS | Wide-angle x-ray scattering |
| XPS | X-ray photoelectron spectroscopy |

# Contents

# 1

# Introduction

Nanocelluloses are materials that are comprised of nanosized fibrils and rod-like particles. These materials have outstanding properties, namely high mechanical strength, the ability to form networks in aqueous media, abundant hydroxyl groups and semi-crystallinity [1]. Moreover, the biodegradability, renewability, non-toxicity and low density of nanocelluloses are significant assets in, for example, composite and medical applications. They have therefore been in the spotlight of the biomaterials community in the last decade, where many functions, such as viscosity modifiers, membranes and wound dressings, have been proposed [2, 3]

There are different types of nanocelluloses: bacterial nanocellulose, algal cellulose, cellulose nanofibers (CNF), cellulose nanocrystals (CNCs), and tunicate CNCs [4]. From them all, commercially-available CNCs are used in the present study. The CNC properties depend on the source and manufacturing procedure. CNCs can be produced by various routes, such as acid hydrolysis, oxidation and enzymatic hydrolysis or produced with ionic liquids or sub-critical water [5] adding selected functionality on the surface. Most industrially available CNCs are produced from cellulose by sulfuric acid hydrolysis. The sulfuric acid hydrolyses the glycosidic bonds in the less ordered regions of cellulose and esterifies some hydroxyl groups present on superficial cellulose molecules, leaving highly crystalline nanoparticles. The surface of the CNCs is composed mainly of hydroxyl and some sulfate half-ester groups.

Cellulose, and consequently CNCs, can be modified chemically either via their abundant hydroxyl groups or reducing end-groups of the cellulose chain [6]. Periodate oxidation is a common functionalization for introducing aldehydes to the

CNC surface, resulting in dialdehyde cellulose (DAC) or reducing further into alcohols and an open ring structure [7]. Periodate oxidation cleaves the C2 - C3 (carbon in Positions 2 and 3) bond in the anhydroglucose unit (AGU) and transforms them both into aldehydes and further hydrated aldehydes in water, such as hemiacetals or hemiadals [8]. The aldehydes are used to crosslink networks or to react with other functionalities that increase the uses of the DAC, such as UV absorbing molecules [9].

Nanocelluloses form entangled networks in the water interacting electrostatically, via hydrogen or covalently (through functionalities), which reinforce three-dimensional networks [10, 11] and are to form hydrogels. Gelatin is often an employed partner for preparing hydrogels with nanocelluloses. CNF with carboxylic acid functionality mixed with gelatin increased the hardness of the gel until percolation was achieved at 0.5 wt% CNF content [2]. Moreover, the amine groups of the gelatin were used to react with the aldehydes of the DAC [12, 13]. The chemical crosslinking resulted in an increase in the modulus and thermal stability of the gelatin gels [14].

Self-sustaining gels are commonly used in medical applications. In microwave treatment and diagnostics, many types of gels including gelatin, agarose or carrageenan has been used to create materials that mimic tissue for verification, quality assurance (QA) procedures and dosimetry. In order to mimic the fat tissue, which is the focus of this thesis, gelatin was used in the matrix to enclose other materials, such as oil in an emulsion [15, 16]. The result is a material that possesses characteristics equivalent to real tissue that is present in a human body, such as dielectric equivalences, and is referred to as a “phantom”.

Replicating materials that mimic fat tissue, i.e. fat phantoms, has been challenging. The dielectric properties of fat tissue require a low content of water, which is used as matrix. The lack of matrix means, in turn, that the material will have insufficient structural strength. There is therefore a need for a strong network that is able to enclose high oil ratios, for which gelatin is an ideal candidate. The challenge facing the use of gelatin in therapeutic and diagnostic systems, however, is often its low melting point ($<28\ ^{\circ}C$); a problem that could

be solved by using toxic crosslinkers, such as formaldehyde (Acute oral toxicity ($LC_{50}$): 42 mg/kg (Mouse) [17]) [18].

The work in this thesis contributes to the development of wood nanoscience and nanotechnology. It is focused on the oxidative modification of CNCs by periodate to facilitate the network formation that was applied in hydrogel formation, and demonstrated as a matrix in fat phantoms. The general objective here is to elucidate the variables of oxidation of commercial CNCs that consist of a substantial amount of (presumably) non-oxidizable sulfate half-ester functionalities. The intrinsic character of the oxidation and resulting product are presented via physico-chemical characterization of the oxidation reaction. The hypothesis is that the sulfate half-ester groups not-only affect the oxidation kinetics but also the colloidal properties of the product, hence detailed insight into chemical characteristics of both are essential for any utilization of periodate oxidized CNCs. The oxidized CNCs are subsequently applied to be used as a chemical crosslinking moiety in gelatin networks to circumvent the use of toxic crosslinkers. The reinforcement of the CNCs in the network formation is observed and the applicability to fat tissue matrix material is demonstrated.

# 2

# Background

## 2.1 Cellulose nanocrystals and their surface properties

The abundant surface hydroxyl groups present on the CNC particles allow functionalization that adapts the surface properties for various targeted applications [19, 20]. Functionalization with aldehydes on the surface of the CNCs can generate a versatile portfolio of polysaccharide hierarchies [21].

Periodate oxidation and further reduction/oxidation leads to alcohol and carboxyl derivatives [7, 22, 23, 24] which are used for modifying the thermal and mechanical properties of cellulose materials [25, 26]. The periodate oxidation of crystalline cellulose typically leads to degradation occurring simultaneously with chemical modification [19]. It has been reported that the crystallinity of cellulose decreases with oxidation [27]. Temperature accelerates oxidation, leading not only to an increase in reaction rate but also to accelerated degradation [27]. It has been proposed that degradation of the crystalline regions takes place heterogeneously, leading to oxidized clusters [28]. Peeling off of the surface layer has been demonstrated as being a result of the oxidation, as evidenced by altered CNC dimensions [29] and in Nuclear Magnetic Resonance (NMR) spectroscopy analysis [30]. The overall crystallinity has been found to be a determining factor of the oxidation rate [31], although the crystallinity of the starting materials also plays a role [32]. Oxidation of crystalline cellulose has been reported to proceed heterogeneously, leading to local loss of order and isolated oxidized domains. Indeed, the highly-ordered regions in cellulose are reported to be affected already at a low degree of oxidation (DO) [33, 34].

It is often the case that the hydroxyl groups dominate when the properties and modification of cellulose and CNCs are considered. However, the production of CNCs also introduces a sulfate half-ester group on the surface: a group that is comprised of one sulfur atom and four oxygen atoms. The functional group has the structure R-O-$SO_3^-$, where two of the oxygen atoms are double bonded to sulfur and another single oxygen is bonded to an organic chain. In the case of cellulose, the group is bonded to the C6 which is the most reactive carbon in the molecule [35].

The amount of sulfate half-ester groups can be controlled. On the one hand, the amount of the functional group can be increased by adding sulfuric acid and heating it for 2 h at 40 °C [36] and on the other hand, the amount of the sulfate half-ester groups can be decreased via hydrochloric acid-catalyzed desulfation by adding hydrochloric acid at 80 °C with constant stirring for 2.5 h.

The sulfate half-ester group provides a net negative charge in pH 2 $>$ providing colloidal stability. Colloidal stability is essential in engineering applications to disperse them in water and to prevent aggregation. The sulfate half-ester groups can be used to react with azetidinium salts increasing the hydrophobicity [37]. Azetidinium conjugation could fine-tune some material properties since azetidinium ions can be designed in many varieties [37].

## 2.2 CNC-gelatin networks

Gelatin forms a random coil conformation in hot water; upon cooling, a self-standing gel is created through the formation of rigid triple helices connected by flexible links [38, 14]. Periodate oxidized CNCs with aldehyde functionality have been used to crosslink or graft with gelatin via the Schiff base reaction [39] which is favored at pH 4 [40] and used by Dash $et\ al.$ [12].

### 2.2.1 Microwave treatment and diagnostics

In this work, CNC-gelatin networks were employed as "phantoms" used during verification procedures of medical devices in microwave treatment and diagnostics. Microwave diagnostics and treatments use microwave devices that have the advantages of being cost-effective, compact and portable while providing fast acquisition. The most clinically utilized application of microwave technology is hyperthermia cancer treatment, in which the temperature of the tumor is increased to a therapeutic level between 40 - 44 °C. This increasing in temperature kills the tumor cells and/or make them vulnerable to other treatment modalities, such as radiotherapy and chemotherapy [41, 42, 43, 44]. Another application of microwave technology in the medical field is the rapid diagnosis of breast cancer, stroke and traumas [45, 46]. Microwave diagnostics utilize the difference between the dielectric properties of healthy and malignant tissues, which allow a fast recognition of health problems.

The development and verification of both the diagnostic and treatment systems require standarized tissue-mimicking materials, i.e. phantoms. A phantom is a physical material that imitates the characteristics of biological tissue in terms of either electromagnetic (EM) wave propagation or the thermal redistribution of heat. It is designed in such way that it provides the same response as real tissue, which is then used to characterize the performance of a device or a method under test. The interaction of EM fields with biological tissue can be predicted by either quantifying the specific absorption rate distributions in the solid phantom or estimating the propagation of the electromagnetic field in a phantom via the measurement of scattering parameters [47, 46]. Although the characteristics desired of the phantom material vary slightly between applications, they often/always include non-toxicity, a simple easy procedure that allows their being made in clinics, being easy to handle and stability. In general, biological tissues, and thus the phantoms, can be identified as belonging to a high water-content or a low water-content group. There are numerous phantoms available that mimic high water-content tissues, such as muscle or brain, while those for low water-content tissues, such as fat or bones, are still lacking. The fat phantom recipes in the literature either used toxic formaldehyde to increase thermal stability or

were unable to be replicated in clinics [18]. The addition of CNC derivatives to the fat phantom recipe could solve the thermal stability problem. The phantoms used in the development and verification would, however, be required to pass a quality assurance test and other verifications prior to implementation [48, 47].

# 3

# Experimental

## 3.1 Modification of CNCs

### 3.1.1 Desulfation

CNC from CelluForce, Canada, was dispersed in water up to a concentration of 5 wt%, after 12 M HCl was added to attain 1.8 M acid concentration. The dispersion was heated under reflux to 90 °C and stirred for 2 hours. The suspension was dialyzed until the pH of the dialysate was the same as the deionized water used for the dialysis. The desulfated CNC grade is referred to as desulfCNC henceforth.

The composition of the sulfate half-ester content was determined using elemental analysis. The number of AGUs present per sulfate half-ester group was calculated by fitting the contributions of AGU, AGUs with a sulfate half-ester at C6 and 2,3-dialdehyde-AGUs to the experimental data obtained from the elemental analysis. The fitting searched the minimum molar percentage error for all the components found in the elemental analysis, with $Na^+$ being excluded from the fitting. Other methods such as FTIR and XPS, were also used in Paper I.

### 3.1.2 Oxidation

A similar oxidization procedure to that used by Dash $et\ al.$ [12] was adapted to the CNCs. A weight ratio of 0.7 sodium metaperiodate to CNC in 0.1 M acetate buffer of pH 4 and 50 mM ionic strength was used, the initial concentration of CNCs was 3 wt% and the DO was controlled by the reaction time. Glycerol was used to quench the reaction. Following oxidation, the suspensions were dialyzed

in order to remove the residual periodate, iodate and glycerol. The dispersions were then stored at 4 °C.

#### 3.1.2.1 Determination of degree of oxidation

The DO during the oxidation reaction was tracked by the consumption of periodate observing the UV absorbance at 290 nm [49]. The DO calculated from UV absorbance was also used as a reference. Other methods, such as NRM spectroscopy, hydroxylamine hydrochloride assay and elemental analysis, were also used in Paper I for determining the DO.

#### 3.1.2.2 Kinetics of oxidation reaction

The dialdehyde cellulose is obtained from the reaction of sodium metaperiodate and C2 and C3 of the cellulose AGU. The reaction is located on the surface of the CNC, and is thus a solid-liquid heterogeneous reaction [27].In order to reduce the level of complexity of the analysis, some assumptions were made to fit the reaction to pseudo first-order kinetics (Equation 3.1, namely: 1) The reaction is slow and not limited by the mass transfer, with no brush formation on the surface that could cause diffusion limitations to further reaction; 2) The reaction is stoichiometrically 1 to 1 and no side reactions take place; 3) There is a linear dependence on the concentration of periodate [$P$] and the CNC concentration [$AGU$] has low impact on the rate ($r$). In Equation 3.1 [$P$] at time $t$; and [$P_0$] stands for the concentration of periodate and its initial concentration, $k'$ is the reaction rate.

$$\frac{[P]}{[P_0]} = e^{-k' \cdot t} \tag{3.1}$$

## 3.2 Determination of zeta potential

Zetasizer nano (Malvern, UK) was used to measure the zeta potential of the dispersions of CNC derivatives. The measurements were performed at 25.0 ± 0.1 °C. The CNC derivatives at 0.25 wt% concentration were measured in 0.1 M acetate buffer at pH 4. The data was processed processed using Zetasizer V7.13 software (Malvern, UK). A total of six measurements of each CNC derivatives

were performed, with each measurement being comprised of 30 to 150 sub-runs. The average of the 6 measurements was taken as the zeta potential.

## 3.3 Wide-angle x-ray scattering analysis

The crystallinity index (CI) and the crystallite were studied using Wide-Angle X-ray Scattering (WAXS) which was performed using Mat:Nordic SAXS/WAXS (SAXSLAB, France); the diffraction patterns obtained were deconvoluted with OriginPro 2021 into Voigt functions. The crystallinity was calculated using the total area ($A$) of the crystalline areas: (101), (10$\bar{1}$), (021) and (002) by the total contribution, which included the amorphous area located at approximately 18° (Equation 3.2). The Scherrer equation was used to determine the crystallite size; a correction factor of 0.9 was used [50].

$$\text{CI (\%)} = \left(1 - \frac{A_{\text{amorphous}}}{A_{\text{amorphous}} + A_{101} + A_{10\bar{1}} + A_{012} + A_{002}}\right) \cdot 100 \tag{3.2}$$

## 3.4 Degree of surface substitution

The surface ratio ($R_s$) was defined as the ratio between the number of surface cellulose chains and the total number of cellulose chains in the CNCs. The $R_{sur}$ was calculated using WAXS data [51, 52].

The degree of surface substitution (DSS) of the DO, $DSS_{DO}$ (Equation 3.3), and the sulfate half-ester groups, $DSS_S$ (Equation 3.4), was defined as the amount of 2,3-dialdehyde-AGUs, and AGUs with the sulfate half-ester at C6, per superficial cellulose chains. The degree of surface sites used, $DSS_U$, was defined as the percentage of the superficial modified AGUs and the AGUs in the actual surface that were modifiable (Equation 3.5). The 180° angle of $\beta$-1,4-glycosidic linked glucose units meant that every other superficial AGU was considered modifiable by oxidation, and each remaining superficial AGU was considered able to host a AGU with a sulfate half-ester group. Thus, the $DSS_U$ was calculated as the number of molecules substituted by the superficial molecules modifiable by each type of modification. In Equation 3.4 $c_S$ is the sulfur molar concentration.

$$\mathrm{DSS_{DO}} = \frac{n_{\mathrm{ox}}}{n_{\mathrm{sur}}} = \frac{\mathrm{DO}}{R_{\mathrm{S}}} \tag{3.3}$$

$$\mathrm{DSS_{S}} = \frac{n_{\mathrm{S}}}{n_{\mathrm{sur}}} = \frac{c_{\mathrm{S}}}{R_{\mathrm{S}}} \tag{3.4}$$

$$\mathrm{DSS_{U}} = \frac{n_{\mathrm{DO}}}{\frac{n_{\mathrm{sur}}}{2}} + \frac{n_{\mathrm{S}}}{\frac{n_{\mathrm{sur}}}{2}} \tag{3.5}$$

## 3.5 Analysis of CNC diameters

### 3.5.1 Atomic Force Microscopy

Atomic Force Microscopy (AFM) is method largely used to determine the diameter distribution of the CNCs. The semi-contact mode, using the AFM (NTEGRA, NT-MDT, Russia) with Tap300AI-G tips, was employed for the characterization of the morphology. The AFM recorded regions of interest, 5 x 5 $\mu$m in size, of CNCs on a silicon wafer (Siegert wafers, Germany). Using Gwyddion 2.56, the images were post-processed by removal of the polynomial background and row aligning. A significant number of potentially single CNC profiles was extracted from of the processed image, a cross-section consisted of 1,000 points.

### 3.5.2 Calculation of CNCs height

CNC profiles were processed using Matlab 2019. The script fitted to an arbitrary order to reduce the noise of the measurement in order to find the inflection points: in this case to polynomial 14th degree was chosen and it is discussed in Chapter 4.4.1. The polynomial was differentiated and the inflection points, only those with a positive change of sign, were listed. The profile was divided into sections according to the inflection points. The average height of each section was calculated, and the highest was considered as being the main section.Moving outwards from the main section, the average height of each adjacent section was compared to its inflection points. If the average height of the section was lower, the main section was increased until the inflection point the end of that

section. The inflection points of the main section were considered to be the bottom points of the peak and were used for baseline correction; the height was calculated perpendicular to the corrected profile.

## 3.6 Preparation of phantoms

Oil and water were heated separately to 60 °C for the gelatin-stabilized emulsion. Lecithin B-10 (Dupont, Denmark) was dispersed in the water phase and left to mix for 10 minutes. The gelatin, Bloom 296 Gelatin A (Gelita, Sweden), was then added and mixing continued for a further 20 minutes. When the lecithin and gelatin were mixed, the oil was added dropwise under vigorous stirring using Ultra-turrax (IKA T50), which resulted in a system that was visually turbid.

In the case of CNC/DAC (DO 14 %) reinforced gelatin stabilized emulsions, the procedure was similar to the gelatin emulsions except that the dispersion of CNC or DAC was heated to 50 °C before being added to the highly concentrated gelatin-water system, and the the oil was incorporated dropwise.

The concentrations given in weight percent of the emulsions , were of
70 % oil, 2 % gelatin, 0.6 % lecithin, 0.6 % CNC derivative (if required) and the remainder was water.

## 3.7 Rheology

The rheological properties of the emulsions were determined using a DHR-3 rheometer from TA Instruments, Denmark. The geometry used was plate-plate (40 mm in diameter) with a gap of 1 mm. The upper plate was equipped with a solvent trap and used with a custom-made evaporation chamber from TA Instruments. The samples were added to the plate at 60 °C , the upper plate was lowered to the measurement position and the temperature was reduced to 10 °C with a rate of 2 °C $min^{-1}$ and kept at 10 °C for 5 min. The temperature was then increased to 60 ° at a rate of 2 ° $min^{-1}$. The storage (G') and loss (G") moduli of

the samples were recorded at a frequency ($f$) of 1 Hz and a strain of 0.5 %. The sol-gel transition was defined at the temperature where G" crossed over G'. The temperature was controlled by means of a Peltier plate.

## 3.8 Testing for compliance with QA guidelines for superficial hyperthermia

The set up used to evaluate the performance of fat phantoms during the hyperthermia QA procedure is as described in Trefna $et.al.$ [47, 48]. The arrangement was as follows: a self-grounded bow-tie antenna was placed in a water-filled plastic enclosure that positioned on a 15 mm thick hydrogel bolus to assure a proper transmission of the microwave energy to the two-layered phantom [53]. The top layer, representing fat tissue had a thickness of 10 mm and was placed on a muscle phantom of thickness 70 mm [54]. The experiment was carried out at a room temperature of around 20 °C. A power of 60-63 W was applied to the antenna port for 6 minutes whilst the water within the antenna enclosure was circulated to ensure a constant temperature of 20 °C. The temperature distribution at the surface of the top layer of the fat phantom was measured by an infrared camera (IR) (B355, FLIR Systems, USA) immediately after the power supply was shut off. Further details can be found in Paper II.

## 3.9 Statistical analysis

The software OriginPro 2021 was used for the non-linear fittings, including the R-square or coefficient of determination (COD), descriptive statistics and F-test. The variations are considered significant at P-values less than 0.05.

# 4

# Results and Discussion

In the objective of understanding the function of the sulfate half-ester group in the oxidation reaction, the kinetics of the reaction were studied using two different starting sulfate half-ester content on the CNCs. The reaction rate were calculated following the periodate concentration. Elemental analysis, FTIR and XPS were used to characterize the sulfur contents of the reactants and products of the reaction in order to monitor the sulfate half-ester content through the reaction; UV absorbance, titration, elemental analysis and NMR spectroscopy were used to determine the DO. The changes in the surface charge, and thus the colloidal properties, were also studied via the zeta potential. The variations in morphology of the resulting CNCs due to the reaction were measured using AFM for the diameter distribution and WAXS for the crystallinity. Together with the calculation of the superficial sites used by these surface modifications, it was apparent that the modification was possibly located elsewhere than on the surface of the CNCs. Moreover, the aldehyde functionality on the CNCs obtained from the oxidation reaction was used to crosslink the amine groups of the lysine in the gelatin network of oil-in-water emulsions. The reinforcement of the network was characterized by rheology measurements that studied the strength of the solidified emulsions at different temperatures. Finally, a proof-of-concept test for the hyperthermia treatment was performed.

## 4.1 CNC derivates

The starting sulfur content in wt% of the CNC grades studied is reported in Table 4.1. It was calculated, from the fitting the monosaccharides to the elemental analysis, that the CNCs had one sulfate half-ester group residing in every 18th glucose unit. The grade with a lesser amount of sulfate half-ester, desulfCNC,

was obtained after desulfating the starting CNCs with HCl. The desulfCNC presented a decrease down to one sulfate half-ester group in every 69th glucose unit.

**Table 4.1:** Elemental analysis of sulfur present in the CNCs, expressed as wt%. The standard deviation was less than 0.02. The percentage next to the CNC grade is the degree of oxidation determined by UV absorbance.

| *Specimen* | **S** |
|---|---|
| **CNC** | 1.09 |
| **DAC 12 %** | 0.71 |
| **DAC 29 %** | 0.69 |
| **DAC 57 %** | 0.66 |
| **desulfCNC** | 0.29 |
| **desulfDAC 13 %** | 0.30 |
| **desulfDAC 33 %** | 0.26 |
| **desulfDAC 53 %** | 0.24 |

## 4.2 Oxidation reaction

CNCs with varying amounts of sulfate half-ester group were oxidized via periodate reaction to study weather or not any difference could be observed. The reaction was monitored $insitu$ following the periodate oxidation using UV absorbance (Figure 4.1). In the Figure 4.1, the CNC with a higher concentration resulted in a slower rate. For comparison, the kinetics were studied fitting the data to pseudo-first-order kinetics.

The calculated reaction rate for the oxidation of CNC, $k_1'$, was the following: -1.98 $\cdot$ 10 $^{-5}$ $\pm$ 1 $\cdot$ 10$^{-6}$ s$^{-1}$. The reaction rate for the oxidation of the desulfCNCs, $k_2'$, was -5.09 $\cdot$ 10$^{-5}$ $\pm$ 4 $\cdot$ 10$^{-6}$ s$^{-1}$, which was higher than that of the CNCs. Both regressions were considered acceptable according to the

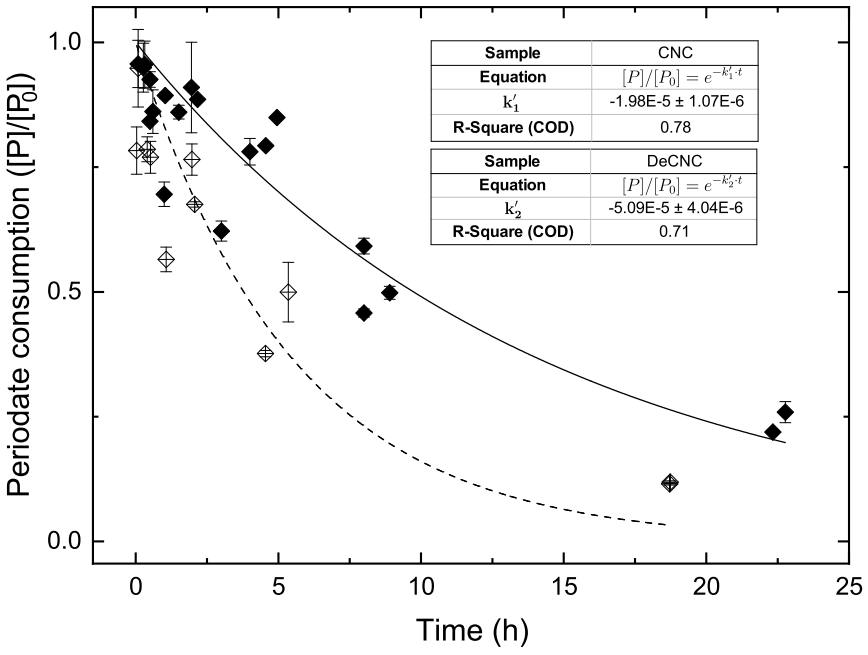


**Figure 4.1:** Consumption of periodate during oxidation of CNCs (◆) and desulfCNCs (⊕). The equations containing $k_1'$ and $k_2'$ correspond to CNC and desulfCNC respectively. R-square i.e. the coefficient of determination (COD),is a statistical measure for qualifying the regression. These curves are comprised of three oxidation series for each CNC derivative. Although some points are excluded here for the sake of clarity, they are included in the fitting and statistical analysis.

R-square. The agreement on the consumption of periodate, especially at the beginning of the reaction, indicated that the CNC had small influence on the rate, and the approximation to a pseudo first-order could therefore be correct. The calculated reaction rates were statistically different according to the F-test. The decrease in the amount of sulfate half-ester groups on the surface increases the reaction rate by approx. 150 %. The oxidized CNC and desulfCNC grades are referred to as DAC and desulfDAC, respectively.

Periodate oxidation also altered the elemental composition of the CNCs alongside the reaction, as shown by the elemental analysis in Table 4.1 and also by FTIR and XPS in Paper I. The sulfur content decreased with oxidation, suggest-

ing that the sulfate half-ester groups were removed from the surface. The oxidation modification added aldehyde functionalities to the surface of the CNCs, the quantity of which was measured by NMR spectroscopy, hydroxylamine assay and FTIR, discussed in Paper I. The aldehyde functionalities were used with gelatin to form entangled networks through the Schiff base reaction, see Paper II.

## 4.3 Colloidal properties

CNCs are colloidally stable, which is often given by the negative charge of the sulfate half-ester groups on the surface. Zeta potential is a measurement that allows the colloidal stability to be compared. In Figure 4.2, the zeta potential measured of the starting CNCs was -27.6 mV. Desulfation removed the charges from the surface and thereby increased the zeta potential to -19.3 mV. Oxidation resulted in an increase in the zeta potential of both grades. When the DO was approx. 50 %, the zeta potential of both grades was approx. -5 mV, which was similar even when the amount of sulfate half-ester groups calculated from the elemental analysis was not the same. The zeta potential manifested the colloidal instability of both the desulfCNC and the highly oxidized grades.

## 4.4 Characterization of CNC morphology

The effects that the desulfation and oxidation had on the morphology of the CNCs were studied by measuring the size using AFM and calculating the crystallinity using the patterns obtained by WAXS.

### 4.4.1 Analysis of CNC diameters

AFM is a commonly-used method employed to measure the diameter of CNCs. However, the lateral aggregation of particles and presence of multiple CNCs in what appears to be individual CNCs contribute to the large asymmetry in cross-sections [55]. Accordingly, particle selection appears to be the main source of variation between analysts [56].

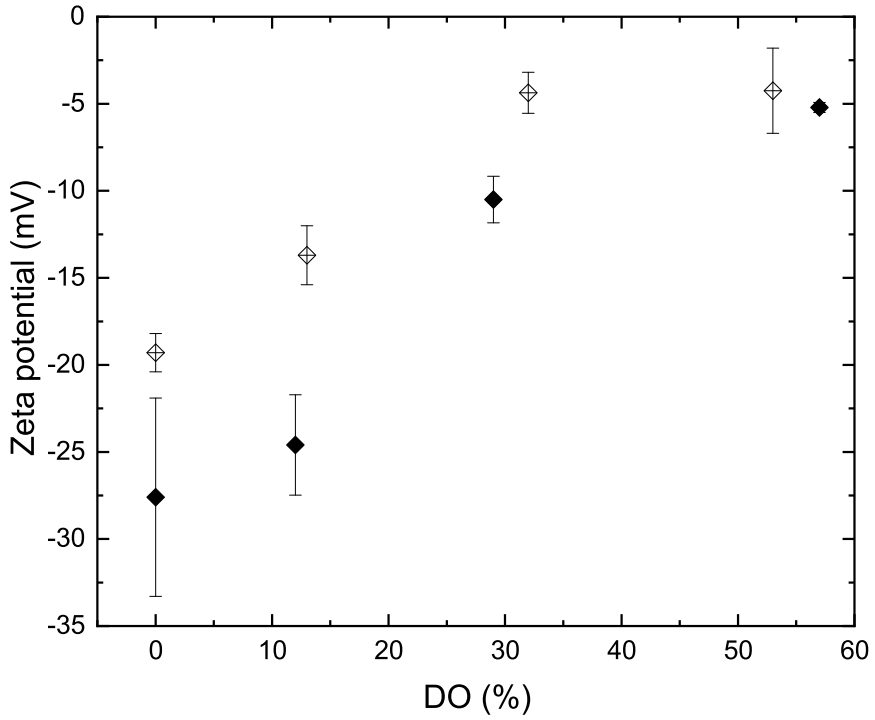


**Figure 4.2:** Zeta potential of CNCs (◆) and desulfated CNCs (⊕) with varying DO.

A significant amount of CNCs has therefore to be measured in order to decrease the error when characterizing the diameter distribution: a Matlab script was developed with the intention of examining as many diameters as possible. The script read the profiles from a data file created by Gywyddion. The profiles were fitted to an arbitrary polynomial degree, in this case a 14th degree, with the purpose of localizing the peak and its base points based on derivatives. The profile was then baseline corrected and the peak height measured. With the aim of verifying all the calculations manually, plots such as the one shown in Figure 4.3 were used: the original profile resulting from the AFM is shown as blue dots, and the fitting as the red dashed line. The inflection points, i.e. the points where the function grows, are marked by red circles. The baseline, in green, connects the two inflection points where the function does not grow further. The black dashed line is perpendicular to the baseline where the height of the profile was calculated. If the chosen height was not deemed as being optimal (Figure 4.3),

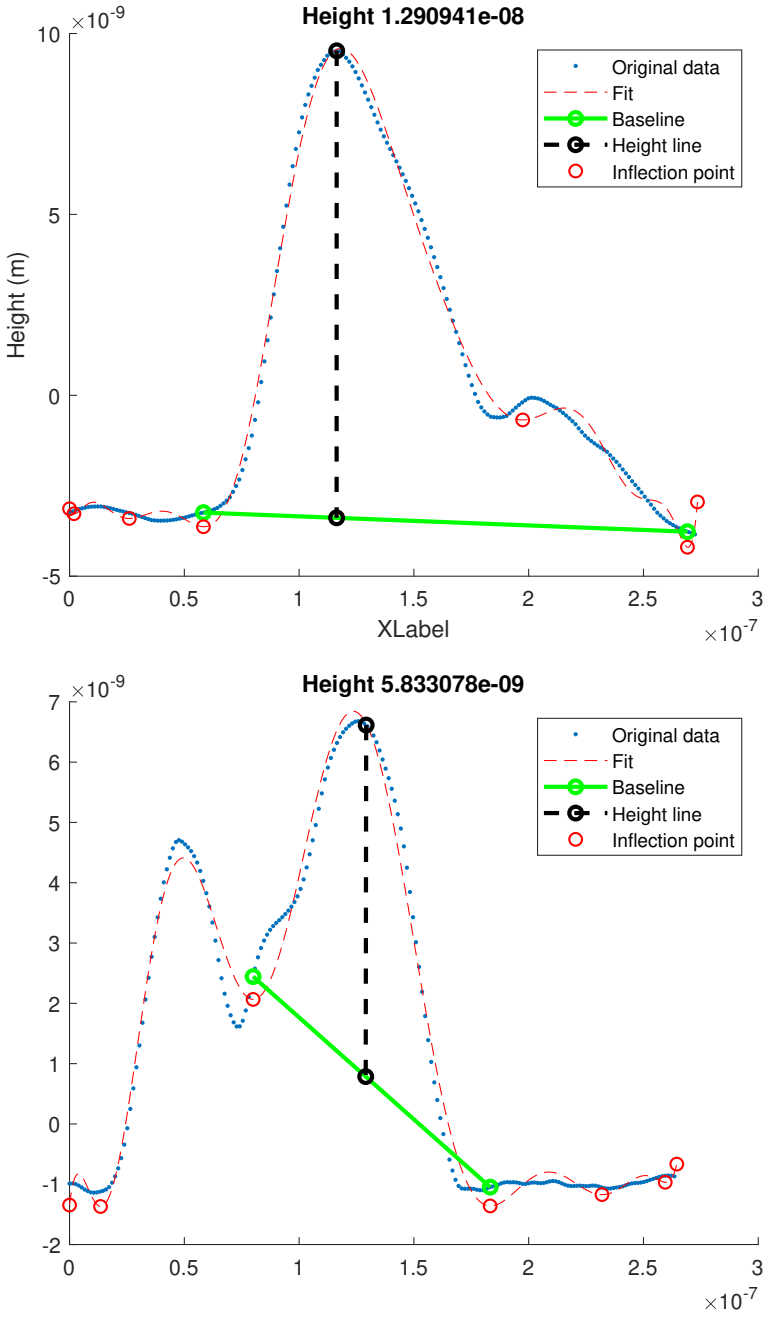


**Figure 4.3:** Above: a successful height calculation, shown by the dashed black line. Below: a non-successful height calculation and therefore subsequently calculated by OriginPro.

then a height was calculated manually using OringPro. A successful calculation was considered when the baseline was set at the bottom of the full profile and followed the background profile.

The polynomial degree chosen could affect the baseline correction and thus the final result but, as discussed earlier, particle selection is the most influential variable. A sample of 112 profiles was fitted to polynomial 3rd to 40th degree in order to show the slight difference between different polynomial degree fittings. The use of a higher polynomial from the 14th to 30th degree had an average difference of 3 % to the polynomial 40th degree (Figure 4.4) when this was used as a control figure. It is important to note that the polynomial 40th degree fitting does not assure a perfect result and that it was used just for the purpose of comparison.

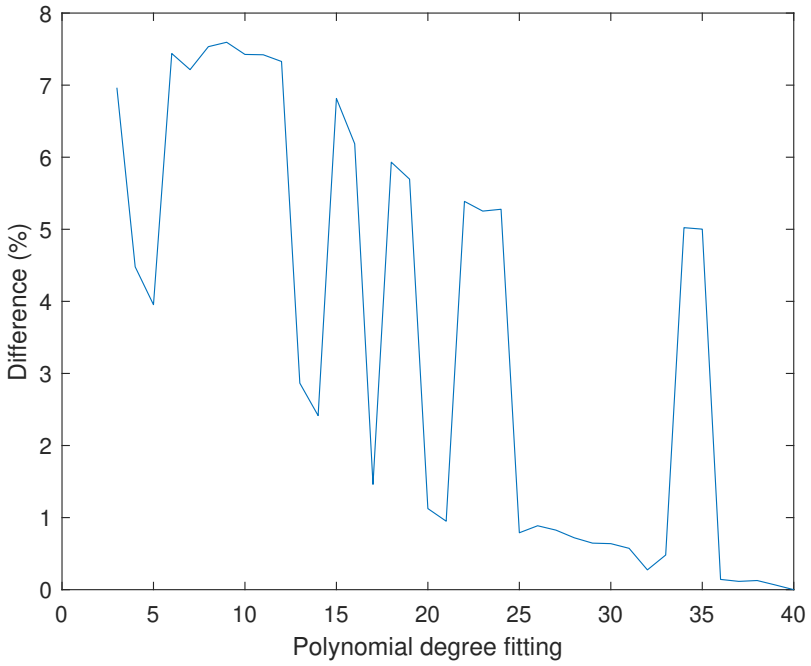


**Figure 4.4:** Differences between various fittings of polynomial degree compared to the fitting with a polynomial 40th degree.

### 4.4.2 Morphological measurements

The method described previously was employed to measure the size of the various CNC grades to discover whether any of the modifications caused changes to the morphology of the particles (Table 4.2). The results were also compared with the crystallite size obtained by WAXS analysis. From the WAXS analysis the ratio between the surface cellulose chains and the total chains and the crystallinity was calculated.

**Table 4.2:** Morphology analysis of the CNCs.

| **Specimen** | **AFM height (nm)** | **Crystallite size ($L_2$) (nm)** | **CI (%)** |
|---|---|---|---|
| CNC | 4.1 ± 1.0 | 5.8 | 81 |
| desulfCNC | 4.0 ± 1.5 | 5.6 | 95 |
| DAC | 3.0 ± 0.8 | 3.4 | 49 |
| desulfDAC | 4.5 ± 1.0 | 3.9 | 63 |

The AFM characterization showed that the size of the CNCs was not affected by desulfation. The difference in size between the CNC and the DAC was statistically significant, however, could indicate that the sulfate half-ester groups were peeled off. The size of the desulfDAC resulted in an increase in size and the difference was not statistically significant with the non-oxidized grades. The lateral aggregation of particles could nevertheless have contributed to increasing uncertainty when determining the diameter, stated previously (Section 4.4.1). Moreover, the desulfDAC had a zeta potential higher than -20 mV (Figure 4.2) which indicates that the particles could aggregate. The crystallite size measured by WAXS showed a decrease in size after oxidation. The comparison made of the diameter measured by AFM and the crystallite size could suggest that the CNCs could be mono-crystalline in that direction. The higher value of the crys-

tallite size suggested that the particles selectied for the AFM analysis, which was aimed at avoiding aggregated particles, mostly measured diameters in the lower quartile of the real size distribution. The desulfation increased the crystallinity, which is explained by the use of HCl: the addition of the acid cleaved any amorphous regions around the CNCs, showing a higher degree of crystallinity. The oxidation decreased the crystallinity of both CNC grades [33, 34], which could be explained by cluster oxidation [28].

## 4.5 Degree of surface substitution

The amount of chains present on the CNC surface can be calculated by the relation between the sizes of the crystallite and the unit cell, which is the distance between cellulose chains, thereby allowing the degree of modification on the surface to be calculated. Table 4.3 shows how the degree of surface substitution (DSS) for the two functionalities, namely sulfate half-ester group $DSS_S$ and dialdehyde $DSS_{DO}$, changed with desulfation and oxidation. The $DSS_{DO}$, increased with the oxidation, as expected; even the fraction of chains on the surface increased with oxidation due to the crystallite size decreasing whilst the cell unit remained the same. The $DSS_S$ decreased with both desulfation and oxidation. The results obtained agree with [57], where the $DSS_S$ was measured for CNCs similar concentrations of sulfur.

The key point here is that oxidation was located not only on the CNC surface, the explanation being that all surface cellulose AGU cannot be oxidized due to the alternate position of the cellulose chain. The degree of surface sites used ($DSS_U$) was calculated, and confirmed that the amount of AGUs that could be oxidized surpassed that available on the surface.

## 4.6 CNCs reinforcing hydrogels

Oil-in-water emulsions, with gelatin as solidifier, have been used in verification procedures of medical devices in microwave treatment and diagnostics. How-

**Table 4.3:** Distribution of the moieties on the surface of the CNC derivates. S: number of AGU for each sulfate half-ester group. DO: degree of oxidation. $R_S$: number of molecules on the surface per total molecules. $DSS_S$: degree of surface substitution of S on total molecules on the surface. $DSS_{DO}$: degree of surface substitution of sulfur on total molecules on the surface. $DSS_U$: degree of surface needed to achieve such an amount of moieties on the surface.

| **Speciment** | **S** | **DO (%)** | $R_{sur}$ **(%)** | $DSS_S$ **(%)** | $DSS_{DO}$ **(%)** | $DSS_U$ **(%)** |
|---|---|---|---|---|---|---|
| CNC | 18 | 0 | 38 | 15 | 0 | 30 |
| desulfCNC | 69 | 0 | 38 | 3.8 | 0 | 7.7 |
| DAC | 30 | 57 | 56 | 6.0 | 102 | 215 |
| desulfDAC | 84 | 53 | 53 | 2.2 | 100 | 205 |

ever, the low melting temperature of the gelatin limited its use. The use of CNC was proposed in Paper II with the aim of increasing the melting temperature of the hydrogels. Their impressive ability of reinforcing the structure of water-rich fluids at low concentrations was expected to contribute to the formation of a stable gel at higher temperatures. Moreover, DACs were also proposed to strengthen the gelatin network by covalent bonding via Schiff base reaction. The Schiff base reaction, in the present case, is the reaction between the dialdehyde functionalization on the CNC surface and the amine groups present on the gelatin. Chemically-bonded junctions form thermally irreversible hydrogels (Figure 4.5), thus providing a network with stability at higher temperatures.

Rheology was used to measure the strength of the network at different temperatures. Figure 4.6a shows the rheological measurements for an oil-in-water emulsion with gelatin as a solidifier. Figures 4.6b and 4.6c show the rheological measurements made when CNC and DAC, respectively, were added as reinforcement. A typical hysteresis in the modulus curve of the gelatin can be observed

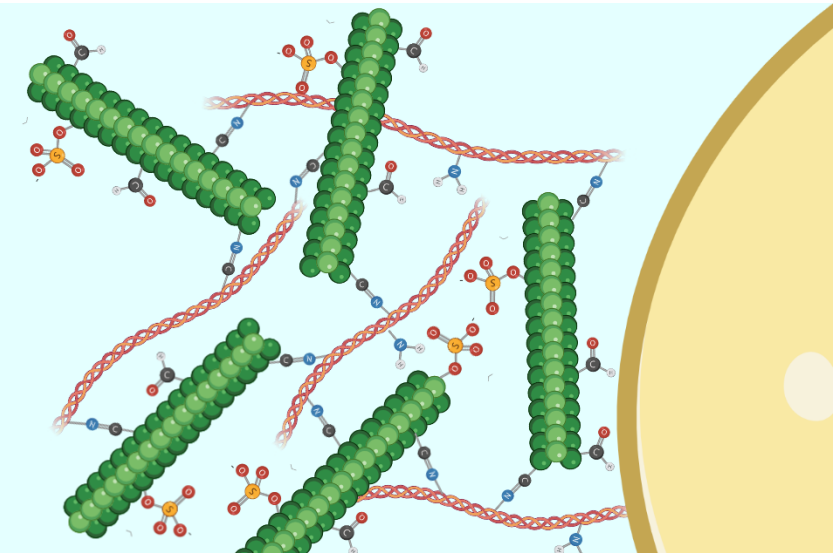

**Figure 4.5:** Schematic illustration of the covalent network in an oil-in-water emulsion, where the yellow represents a droplet of oil and the blue background is water. The covalent network is formed by CNC (green) and gelatin (red) via the aldehydes and amines groups present, respectively. The charged half-esters groups provide the colloidal stability. Created with BioRender.com

[58] in all of these figures: hysteresis behavior appears when the energy needed to entangle or disentangle a network differs. The influence of temperature on the moduli of the gelatin stabilized emulsion shows distinct sol-gel transition at 28 °C upon cooling and gel-solid at 38 °C upon heating (Figure 4.6a). The emulsion stabilized only by gelatin can thus be defined as a liquid at T > 38 °C. However, both of the CNC reinforced gels showed an overall higher G' at higher temperatures. Nonetheless, the CNC and DAC-reinforced emulsions also weakened with temperature as the difference between G' and G" decreased at T > 28 °C and no gel - sol transition was observed at 38 °C. The reinforcement caused by the addition of CNC could be explained by the electrostatic attraction between the negatively-charged CNC and the positively-charged gelatin. There could be a potentially smaller electrostatic attraction in the case of DACs added in the gelatin matrix, since DAC showed less negativity in zeta potential (Figure 4.2) or even aggregation. The DAC aggregates could lead to a non-optimum interconnected network, thus emphasizing the importance of the amount of sulfur present in the DAC. The DAC network is reinforced, not only physically like the CNC-gelatin matrix but also by a covalent bond between the aldehyde of the

DAC and the amine groups on the gelatin. Thus, additions of both CNC and DAC to gelatin provided an increase in thermal stability within the temperature range.

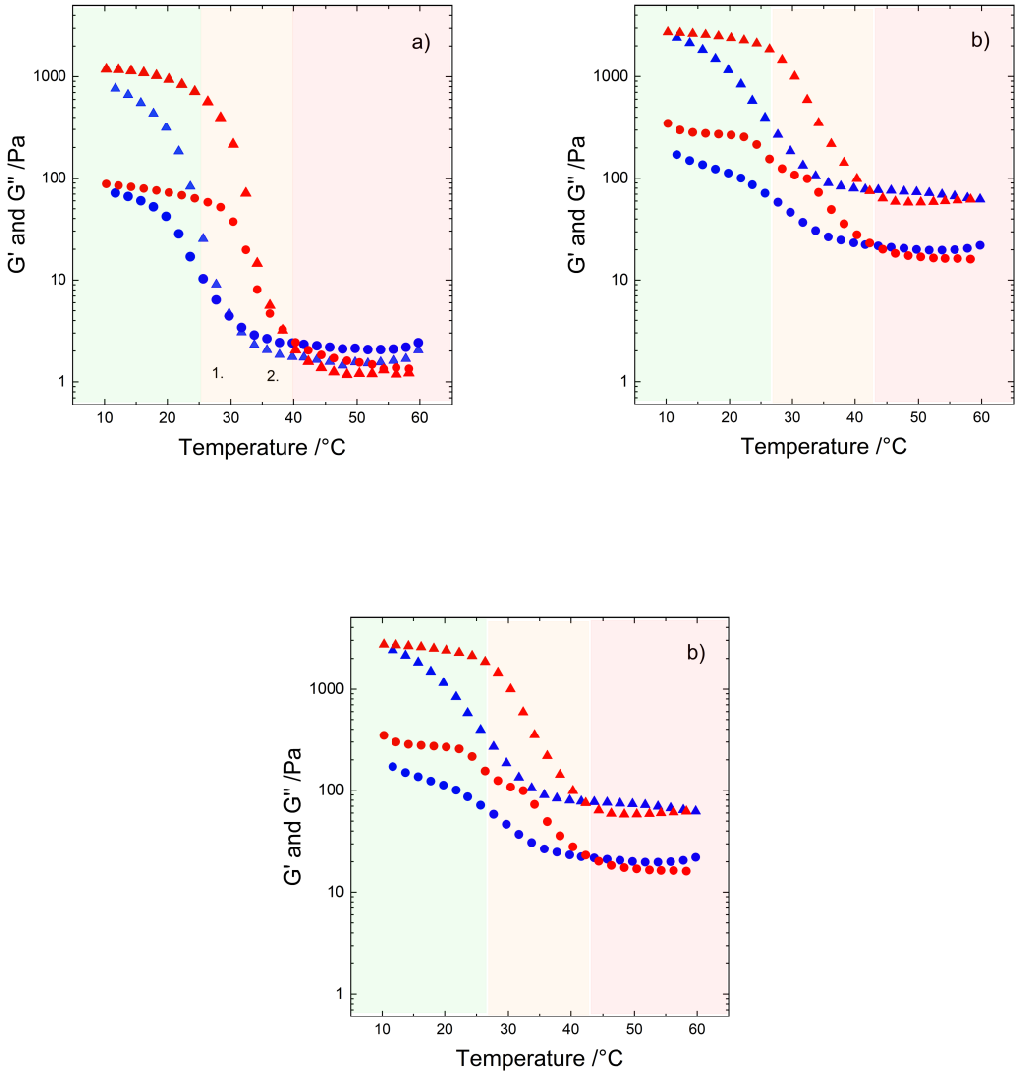


**Figure 4.6:** G' (▲) and G" (●) moduli as a function of temperature for a) gelatin b) CNC-gelatin and c) DAC-gelatin stabilized emulsion. The samples were added at 60 °C, followed by measurements of cooling (blue symbols) and heating (red symbols) performed at $f = 1$ Hz and strain 0.5 %.

The increased thermal stability of the CNC or DAC-reinforced phantoms allowed for a realistic evaluation, via QA procedure, of superficial hyperthermia developed by Trefna *et al.* [45, 44]. The procedure prescribes a setup for, and the execution of, the experimental assessment of applications used for the treat-

ment of superficial hyperthermia, and is explained in detail in Paper II.

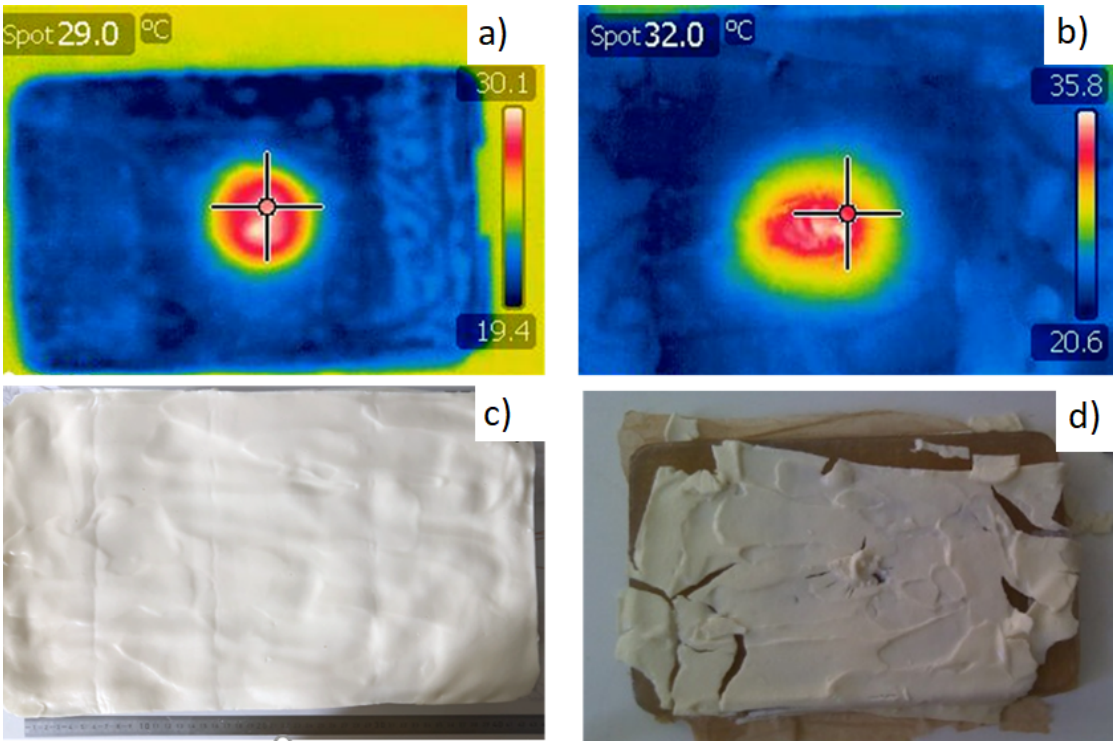


**Figure 4.7:** Temperature distribution on the surface of the fat phantoms reinforced by a) CNC-gelatin b) DAC-gelatin obtained by a infrared camera after the QA procedure test. Images of the fat phantom after the QA procedure test for c) CNC-gelatin and d) DAC-gelatin.

The temperature distribution on the surface of the fat phantom, as characterized by the IR camera, from QA test showed that the CNC and DAC-reinforced phantoms achieved up to approx. 30 °C and 36 °C, respectively (Figure 4.7). The reinforced phantoms exhibited a solid-like behavior in the QA test that was in agreement with the rheological measurements. However, the DAC phantom broke down whilst being handled. The figure also shows that the phantoms were not damaged by the conditions to which they were exposed, thereby successfully reinforcing the original gelatin network expanding the range of applications of the CNC derivates. The successful QA verification of the CNC-gelatin (see Paper II) shows its potential to be used as fat phantom.

# 5

# Conclusions

The role of sulfate half-ester groups in the periodate oxidative reaction and its products has previously not been elucidated. These half-ester groups are present in most of the CNCs available industrially, so understanding their impact is crucial to the efficient production of dialdehyde cellulose in many areas, e.g. the paper industry and the medical field. In this thesis, the oxidation rate of starting materials with varying contents of sulfate has been analyzed, and further characterization of the resulting products performed. Furthermore, CNC derivatives were used to reinforce an emulsion that was solidified by a three-dimensional gelatin network. The emulsion was used in a proof-of-concept test in the biomedical field of microwave treatments.

The presence of sulfate half-ester groups slowed down the rate of oxidation significantly (Figure 4.1). Moreover, the sulfate content of the CNCs containing both high and low levels of sulfate half-ester groups decreased during periodate oxidation (Table 4.2) ), indicating that oxidation leads to desulfation. A significant change in the size of the CNCs was observed for the CNCs (Table 4.2). The crystallinity also decreased upon oxidation, proving that the morphology of the crystals was altered. Finally, a value exceeding 100 % of the $DSS_U$ implies that the modifications were placed elsewhere than on the surface.

The oxidized CNCs were used as a chemical crosslinking moiety in gelatin networks. Rheological characterization of G' revealed that the CNCs and the DAC reduced sensitivity of the gelatin network to temperature. The similar behaviour of CNCs and DAC phantoms in the rheology could not confirm that the DAC network was reinforced by chemical crosslinking, however the observed mechanical properties were different. The lower colloidal stability of the DAC

could, however, have led to aggregates being formed. Such aggregates could not interconnect the whole macro-network chemically but just locally, explaining the lack of difference between the CNC and DAC-reinforced phantoms. It is therefore important that the DO and the colloidal stability in such systems are controlled.

Although fat phantoms reinforced by both CNC-gelatin and DAC-gelatin were shown to be thermally stable for the use in superficial hyperthermia products, only the reinforcement with CNC fulfilled all the requisites in the QA procedure.

From the extensive range of options offered by both functionalities, it has also been possible to identify an interesting feature: optimum amounts of sulfate half-ester and dialdehyde would create a better synergy with the gelatin network and thereby provide a more thermally stable hydrogel. A DAC with an optimum amount of could be obtained taking into account the desulfation of CNCs with periodate oxidation. An outstanding hydrogel could pave the way for the use of this kind of material in other applications, such as scaffolds for organ printing.

# 6

# Outlook

The sulfate half-ester functionality is used with the aim of controlling colloidal stability. This thesis has demonstrated that control is possible not only of the amount of dialdehyde functionality but also of the sulfate-half ester content during the oxidation reaction. Such full control of both functionalities allows for major adaptability of the product through increased efficiency of its manufacture, leading to a new generation of materials that can be produced from trees.

In order to fully comprehend the role of these groups that appear in most industrially-produced CNCs it is recommended that further work be carried out, studying periodate oxidation using different sodium periodate concentrations and sulfate ester concentrations on the surface of the CNCs.

# Bibliography


[1] B. Thomas, M. C. Raj, B. K. Athira, H. M. Rubiyah, J. Joy, A. Moores, G. L. Drisko, and C. Sanchez, *Chemical Reviews*, 2018, **118**(24), 11575–11625.

[2] W. Wang, X. Zhang, A. Teng, and A. Liu, *International Journal of Biological Macromolecules*, 2017, **103**, 226–233.

[3] J. Natterodt, A. Petri-Fink, C. Weder, and J. Zoppe, *CHIMIA International Journal for Chemistry*, 2017, **71**(6), 376–383.

[4] J. George and S. S N, *Nanotechnology, Science and Applications*, 2015, **8**, 45.

[5] O. M. Vanderfleet and E. D. Cranston, *Nature Reviews Materials*, 2021, **6**(2), 124–144.

[6] D. J. Gardner, G. S. Oporto, R. Mills, and M. A. S. A. Samir, *Journal of Adhesion Science and Technology*, 2008, **22**(5-6), 545–567.

[7] P. A. Larsson, L. A. Berglund, and L. Wågberg, *Cellulose*, 2014, **21**(1), 323–333.

[8] I. Sulaeva, K. M. Klinger, H. Amer, U. Henniges, T. Rosenau, and A. Potthast, *Cellulose*, 2015, **22**(6), 3569–3581.

[9] J. A. Sirviö, M. Visanko, J. P. Heiskanen, and H. Liimatainen, *Journal of Materials Chemistry A*, 2016, **4**(17), 6368–6375.

[10] J. M. Jardin, Z. Zhang, G. Hu, K. C. Tam, and T. H. Mekonnen, *International Journal of Biological Macromolecules*, 2020, **152**, 428–436.

[11] B. Wang, J. Liu, K. Chen, Y. Wang, and Z. Shao, *Polymer Engineering Science*, 2020, **60**(4), 782–792.

[12] R. Dash, M. Foston, and A. J. Ragauskas, *Carbohydrate Polymers*, 2013, **91**(2), 638–645.

[13] H. W. Kwak, H. Lee, S. Park, M. E. Lee, and H. J. Jin, *International Journal of Biological Macromolecules*, 2020, **146**, 332–342.

[14] N. G. Parker and M. J. W. Povey, *Food hydrocolloids*, 2012, **26**(1), 99–107.

[15] E. L. Madsen, J. A. Zagzebski, and G. R. Frank, *Ultrasound in Medicine Biology*, 1982, **8**(3), 277–287.

[16] M. Lazebnik, E. L. Madsen, G. R. Frank, and S. C. Hagness, *Physics in Medicine and Biology*, 2005, **50**(18), 4245–4258.

[17] N. C. f. B. I. PubChem [Internet]. Bethesda (MD): National Library of Medicine (US), Pubchem compound summary for CID 712, formaldehyde.

[18] E. L. Madsen, M. A. Hobson, H. Shi, T. Varghese, and G. R. Frank, dec , 2005, **50**(23), 5597–5618.

[19] B. Sun, Q. Hou, Z. Liu, and Y. Ni, *Cellulose*, 2015, **22**(2), 1135–1146.

[20] M. A. Hubbe, P. Tyagi, and L. Pal, *Nanopolysaccharides in Barrier Composites*, 2019.

[21] T. Nypelö, B. Berke, S. Spirk, and J. A. Sirviö, *Carbohydrate Polymers*, 2021, **252**(June 2020), 117105.

[22] H. Liimatainen, M. Visanko, J. A. Sirviö, O. E. O. Hormi, and J. Niinimäki, *Biomacromolecules*, 2012, **13**(5), 1592–1597.

[23] E. Kontturi, P. Laaksonen, M. B. Linder, Nonappa, A. H. Gröschel, O. J. Rojas, and O. Ikkala, *Advanced Materials*, 2018, **30**(24), 1703779.

[24] T. Nypelö, H. Amer, J. Konnerth, A. Potthast, and T. Rosenau, *Biomacromolecules*, 2018, **19**(3), 973–979.

[25] F. Esa, S. M. Tasirin, and N. A. Rahman, *Agriculture and Agricultural Science Procedia*, 2014, **2**, 113–119.

[26] P. A. Larsson, L. A. Berglund, and L. Wågberg, *Cellulose*, 2014, **21**(1), 323–333.

[27] X. Liu, L. Wang, X. Song, H. Song, J. R. Zhao, and S. Wang, *Carbohydrate Polymers*, 2012, **90**(1), 218–223.

[28] U. J. Kim, S. Kuga, M. Wada, T. Okano, and T. Kondo, *Biomacromolecules*, 2000, **1**(3), 488–492.

[29] K. Conley, M. A. Whitehead, and T. G. van de Ven, *Cellulose*, 2017, **24**(2), 479–486.

[30] T. Koso, D. Rico del Cerro, S. Heikkinen, T. Nypelö, J. Buffiere, J. E. Perea-Buceta, A. Potthast, T. Rosenau, H. Heikkinen, H. Maaheimo, A. Isogai, I. Kilpeläinen, and A. W. T. King, *Cellulose*, 2020, **27**, 7929–7953.

[31] M. Siller, H. Amer, M. Bacher, W. Roggenstein, T. Rosenau, and A. Potthast, *Cellulose*, 2015, **22**(4), 2245–2261.

[32] Y. Sa, A. Aa, S. Aa, and R. Sh, 2016, **10**(6).

[33] A. Potthast, M. Kostic, S. Schiehser, P. Kosma, and T. Rosenau, *Holzforschung*, 2007, **61**(6), 662–667.

[34] A. Potthast, S. Schiehser, T. Rosenau, and M. Kostic, *Holzforschung*, 2009, **63**(1), 12–17.

[35] A. M. Regiani, E. Frollini, G. A. Marson, G. M. Arantes, and O. A. El Seoud, *Journal of Polymer Science Part A: Polymer Chemistry*, 1999, **37**(9), 1357–1363.

[36] J. Araki, M. Wada, S. Kuga, and T. Okano, *Journal of Wood Science*, 1999, **45**(3), 258–261.

[37] M. Börjesson, K. Sahlin, D. Bernin, and G. Westman, *Journal of Applied Polymer Science*, 2018, **135**(10), 45963.

[38] D. Hellio and M. Djabourov, *Macromolecular Symposia*, 2006, **241**(1), 23–27.

[39] K. Kriechbaum and L. Bergström, *Biomacromolecules*, 2020, **21**(5), 1720–1728.

[40] M. Di Giovannantonio, T. Kosmala, B. Bonanni, G. Serrano, N. Zema, S. Turchini, D. Catone, K. Wandelt, D. Pasini, G. Contini, and C. Goletti, *The Journal of Physical Chemistry C*, 2015, **119**(33), 19228–19235.

[41] N. Datta, S. G. Ordóñez, U. Gaipl, M. Paulides, H. Crezee, J. Gellermann, D. Marder, E. Puric, and S. Bodis, *Cancer Treatment Reviews*, 2015, **41**(9), 742–753.

[42] N. Cihoric, A. Tsikkinis, G. van Rhoon, H. Crezee, D. M. Aebersold, S. Bodis, M. Beck, J. Nadobny, V. Budach, P. Wust, and P. Ghadjar, *International Journal of Hyperthermia*, 2015, **31**(6), 609–614.

[43] M. Paulides, H. Dobsicek Trefna, S. Curto, and D. Rodrigues, *Advanced Drug Delivery Reviews*, 2020, **163-164**, 3–18.

[44] R. D. Issels, L. H. Lindner, J. Verweij, R. Wessalowski, P. Reichardt, P. Wust, P. Ghadjar, P. Hohenberger, M. Angele, C. Salat, Z. Vujaskovic, S. Daugaard, O. Mella, U. Mansmann, H. R. Dürr, T. Knösel, S. Abdel-Rahman, M. Schmidt, W. Hiddemann, K.-W. Jauch, C. Belka, and A. Gronchi, *JAMA Oncology*, 2018, **4**(4), 483.

[45] A. Fhager, S. Candefjord, M. Elam, and M. Persson, *IEEE Microwave Magazine*, 2018, **19**(3), 78–90.

[46] M. Persson, A. Fhager, H. D. Trefna, Y. Yu, T. McKelvey, G. Pegenius, J.-E. Karlsson, and M. Elam, *IEEE Transactions on Biomedical Engineering*, 2014, **61**(11), 2806–2817.

[47] H. Dobšíček Trefná, J. Crezee, M. Schmidt, D. Marder, U. Lamprecht, M. Ehmann, J. Nadobny, J. Hartmann, N. Lomax, S. Abdel-Rahman, S. Curto, A. Bakker, M. D. Hurwitz, C. J. Diederich, P. R. Stauffer, and G. C. Van Rhoon, *Strahlentherapie und Onkologie*, 2017, **193**(5), 351–366.

[48] H. D. Trefná and A. Ström, *Physics in Medicine  Biology*, 2019, **64**(11), 115025.

[49] E. Maekawa, T. Kosaki, and T. Koshijima, *Wood research: bulletin of the Wood Research Institute Kyoto University*, 1986, **73**, 44–49.

[50] S. Nam, A. D. French, B. D. Condon, and M. Concha, *Carbohydrate Polymers*, 2016, **135**(November), 1–9.

[51] Y. Habibi, H. Chanzy, and M. R. Vignon, *Cellulose*, 2006, **13**(6), 679–687.

[52] E. Kontturi and S. Spirk, *Frontiers in Chemistry*, 2019, **7**(14), 7764–7779.

[53] P. Takook, M. Persson, J. Gellermann, and H. D. Trefná, *International Journal of Hyperthermia*, 2017, **33**(4), 387–400.

[54] Q. Duan, J. H. Duyn, N. Gudino, J. A. De Zwart, P. Van Gelderen, D. K. Sodickson, and R. Brown, *Medical Physics*, 2014, **41**(10).

[55] M. Chen, J. Parot, V. A. Hackley, S. Zou, and L. J. Johnston, *Cellulose*, 2021, **28**(4), 1933–1946.

[56] A. Brinkmann, M. Chen, M. Couillard, Z. J. Jakubek, T. Leng, and L. J. Johnston, *Langmuir*, 2016, **32**(24), 6105–6114.

[57] N. Lin and A. Dufresne, *Nanoscale*, 2014, **6**(10), 5384–5393.

[58] M. Djabourov, J.-P. Lechaire, and F. Gaill, *Biorheology*, 1993, **30**, 191–205.

# Appended Papers

# Paper I

**The effect of sulfate half-ester groups on cellulose nanocrystal periodate oxidation**

Saül Llàcer Navarro, Koyuru Nakayama, Alexander Idström, Lars Evenäs, Anna Ström and Tiina Nypelö.

*Submitted*

**Manuscript**

# The effect of sulfate half-ester groups on cellulose nanocrystal periodate oxidation

**Saül Llàcer Navarro · Koyuru Nakayama · Alexander Idström · Lars Evenäs · Anna Ström · Tiina Nypelö***

Received: DD Month YEAR / Accepted: DD Month YEAR

**Abstract** Periodate oxidation introduces aldehyde functionality to cellulose. The use of dialdehyde cellulose (DAC) has been demonstrated for crosslinking and as a chemical intermediate towards functionalized cellulose. Commercially available cellulose nanocrystals (CNCs) typically carry a surface sulfate half-ester functionality, which results from their manufacture via sulfuric acid hydrolysis and subsequent esterification. The sulfate half-ester group is a bulky group carrying a net negative charge above pH 2 that modifies the colloidal and electro-chemical properties of the CNCs. Periodate oxidation is regioselective to the bond between carbons in positions 2 and 3 in the anhydroglucose unit while the sulfate half-ester groups are located in carbon in position 6. This regioselectivity could be the reason why the role played by the sulfate half-ester group on modification by periodate oxidation has not previously been elucidated. Here, the influence of the sulfate half-ester on the oxidation of CNCs, which is shown to steer the oxidation kinetics and the properties of the resulting materials, is studied. Conventional physicochemical analysis of the oxidant consumption is accompanied by elemental analysis, Fourier-transfrom infrared (FTIR), X-ray photoelectron (XPS) and Nuclear magnetic resonance (NMR) spectroscopy and Wide-angle x-ray scattering (WAXS) analyses; the zeta potential is used to characterize the colloidal properties of the suspensions and Atomic force microscopy (AFM) for determining particle dimensions. The presence of the sulfate half-ester group decreases the rate of oxidation. However, a degree of oxidation of approx. 50 % leads to a decrease in the content of the sulfate half-ester groups. We demonstrate that the CNC surfaces are affected by the oxidation beyond the C2-C3 bond cleavage: insight into the kinetics of the oxidation process is a prerequisite for optimizing CNC oxidation.

**Keywords** Cellulose nanocrystals · Periodate oxidation · Sulfate half-esters

S. Llàcer Navarro · K. Nakayama · A. Idström · L. Evenäs · A. Ström · T. Nypelö
Department of Chemistry and Chemical Engineering, Chalmers University of Technology, 41296 Gothenburg, Sweden

S. Llàcer Navarro · K. Nakayama · L. Evenäs · T. Nypelö
Wallenberg Wood Science Center, Chalmers University of Technology, 41296 Gothenburg, Sweden

## 1 Introduction

It is only recently that native cellulose has been accessible to nanotechnology due to the heterogeneous morphology and the millimeter size of wood fibers. The development of the liberation of nanosized colloidal cellulose nanocrystals (CNCs) from cellulosic materials via hydrolysis with mineral acids, has transformed these entities into bio-based nanoparticles (Kontturi et al., 2018). Sulfuric acid hydrolysis is employed to digest the most accessible, less organized (*i.e.*, amorphous) cellulose chain arrangements, leading to the liberation of the remaining, more ordered, segments into CNCs. Hydrolysis with sulfuric acid leads to the simultaneous esterification of the CNC surfaces with sulfate half-ester groups (Eyley and Thielemans, 2014). The salt-form (*i.e.*, $Na^+$-CNCs, $K^+$-CNCs) allow drying and redispersing. CNCs have been demonstrated as being suitable for use in nanocomposites, biomedical devices, emulsions and foams, and as rheology modifiers (Sinha et al., 2015; Vanderfleet and Cranston, 2021).

Chemical modification for the functionalization of CNCs utilizes the hydroxyl, sulfate half-ester groups, or the reducing end group (Eyley and Thielemans, 2014; Zoppe et al., 2020). The removal of the sulfate groups is one way of modifying the CNCs (Jordan et al., 2019). By far the majority of modifications make use of the hydroxyl groups of cellulose.

Oxidation is a common reaction for modifying CNCs. Periodate oxidation cleaves the bond in the anhydroglucose unit (AGU) between carbons in positions 2 and 3 (C2 and C3) transforming them into aldehydes and further hydrated aldehydes in water (Nypelö et al., 2021). The aldehyde groups can react with vicinal hydroxyls to form hemiacetals or hemialdals (Sulaeva et al., 2015). Moreover, further oxidation or reduction leads to alcohol and carboxyl derivates (Larsson et al., 2014; Liimatainen et al., 2012; Nypelö et al., 2018), which are used for modifying the thermal and mechanical properties of cellulose materials (López Durán et al., 2018; Larsson et al., 2014). The periodate oxidation of crystalline cellulose typically leads to degradation alongside the chemical modification (Sun et al., 2015) and reduces the crystal size or degree of polymerization. It has been reported that the crystallinity of cellulose decreases with oxidation (Liu et al., 2012). Elevated temperature accelerates oxidation leading to not only an increase in the reaction rate but also accelerated degradation (Liu et al., 2012). Degradation of the crystalline regions has been proposed as occurring heterogeneously, leading to a local loss of order and isolated oxidized domains (Kim et al., 2000). The highly-ordered regions (crystalline) in cellulose are reported to be affected already at low degree of oxidation (DO) (Potthast et al., 2007, 2009). Peeling off from the surface layer has been demonstrated as being a result of oxidation, being evidenced by altered CNC dimensions (Conley et al., 2017) and nuclear magnetic resonance (NMR) spectroscopy analysis (Koso et al., 2020). The determining factor of the oxidation rate has been found to be the overall crystallinity (Siller et al., 2015). The hierarchy (fiber, fibril, crystal) of the starting materials does, however, also play a role here (Yuldoshov et al., 2016).

The sulfate half-ester groups provide colloidal stability to the CNC suspensions because their deprotonation leads to the presence of a negative charge. We

hypothesize that the groups may affect the oxidation reaction as well, since the charge affects the affinity to the oxidants. The bulky sulfate half-ester group may also be a sterical hindrance to the periodate ion in accessing the oxidizable diols. The effect of sulfate half-ester groups on the periodate oxidation of CNCs are elucidated; furthermore, we investigated how the initial content of sulfate half-ester groups affects the properties of the oxidized CNC product. Knowledge of the effect of the sulfate half-ester groups on CNCs and their oxidative modification is pivotal to optimizing the modification of the industrial CNC grades and their employment in nanotechnology.

## 2 Experimental

### 2.1 Materials

CNCs (cellulose sulfate sodium salt) were purchased from Celluforce (Canada). Cellulose is comprised of anhydroglucose units (AGUs) (Figure 1a) and the cellulose sulfate contains a fraction AGUs with a sulfate half-ester substitute (Figure 1b). Sodium periodate, hydroxylamine hydrochloride, glycerol, sodium chloride, sodium acetate, acetic acid, potassium bromide, and hydrochloric acid were purchased from Sigma-Aldrich and used without further purification. MilliQ-water (resistivity = 18.2 $\Omega^{-1}$ $cm^{-1}$ at 25 °C) was obtained from the Millipore water purification system and used unless otherwise stated.

Desulfation of CNCs was performed so that the CNC powder was dispersed in MilliQ-water to a concentration of 5 wt% concentration, after which 12 M HCl was added to obtain an acid concentration of 1.8 M. The dispersion was heated and stirred at 90 °C with reflux for 2 hours. The suspension was dialyzed until the pH of the dialysate was the same as the deionized water used for the dialysis. A spectrapore membrane with a cut off of 12-14,000 g $mol^{-1}$ (VWR, Sweden), was used for dialysis. The desulfated CNC grade is henceforth referred to as desulfCNC.

A procedure from Dash et al. (2013) was adapted for oxidation, whereby the CNCs were oxidized using sodium metaperiodate to a CNC weight ratio of 0.7 in 0.1 M acetate buffer of pH 4 and 50 mM ionic strength and results in dialdehyde cellulose (Figure 1c). The concentration of CNCs was 3 wt%. The DO was controlled by reaction time. Glycerol was used to quench the reaction. After oxidation, the suspensions were dialyzed in order to remove the residual periodate, iodate and glycerol. The suspensions were then stored at 4 °C. As the sodium metaperiodate molecule is larger than the space between the cellulose crystals, the oxidation reaction is expected to take place on the crystal surface, and hence be a heterogeneous reaction Liu et al. (2012). With the aim of decreasing the level of analysis complexity, a number of assumptions were made in order to fit the reaction to pseudo first-order kinetics (Equation 1). These were: *i*) The reaction is slow and is not limited by the mass transfer with no brush formation on the surface causing diffusion limitations to further reaction; *ii*) The reaction is stoichiometric 1 to 1 and no side-reactions take place; *iii*) There is linear dependence on the concentration of the periodate and the CNC concentration has low impact

on the rate.

$$\frac{[P]}{[P_0]} = e^{-k' \cdot t} \tag{1}$$

The pseudo first-order kinetics on the periodate is shown in Equation 1 where $[P_0]$ is the initial molar concentration of periodate, $[P]$ the periodate molar concentration, $k'$ the reaction rate, and $t$ the time.

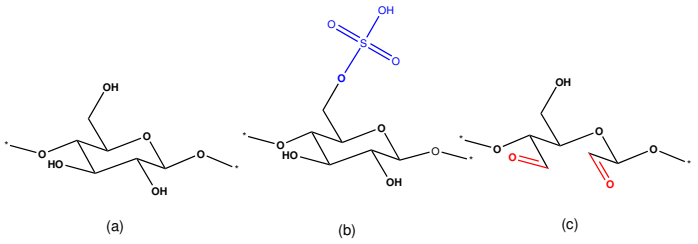


Fig. 1: The structure of a) AGU b) AGU with a sulfate half-ester (blue) at C6 and c) 2,3-dialdehyde-AGU. The aldehyde groups are marked in red.

## 2.2 Methods

Elemental analysis was performed by Mikrolab Kolbe in Germany. The X-ray photoelectron spectroscopy (XPS) analysis was performed using a PHI 5000 VersaProbe III Scanning XPS Microprobe at an angle of 45°. Fourier-transform infrared spectroscopy (FTIR) was recorded using a spectrometer (Perkin-Elmer) and potassium bromide (KBr) tablets were used to carry the specimen. KBr and the analytes were kept at 50 °C for 5 hours to remove water prior to grinding and tableting. The specimens were stored in a desiccator prior to analysis. Wide-angle X-ray scattering (WAXS) was performed using SAXSLab (Mat:Nordic).

Solid-state NMR spectroscopy was performed using a Bruker 400 MHz instrument operating at 100.6 MHz for $^{13}$C with a 3.2 mm solid-state magic-angle-spinning (MAS) probe head. Measurements were conducted at 298 K with a MAS spinning rate of 12 kHz. One-dimensional $^{13}$C Cross-Polarization Magic-Angle Spinning (CP/MAS) spectra were acquired with a 3.0 $\mu$s $^{1}$H 90° pulse, 2000 $\mu$s CP-contact time, 33 ms acquisition time with proton decoupling, and 2 s recycle delay. The number of acquisitions for the CP/MAS spectra was 2048 times with $^{13}$C in natural abundance. Chemical shift were calibrated indirectly through $\alpha$-glycine carbonyl peak (C=O) observed at 176 ppm relative to tetramethyl silane (TMS) at 0 ppm.

The zeta potential of the dispersions was determined using the Zetasizer Nano (Malvern). The measurements were performed at 25.0 ± 0.1 °C and in 0.1 M acetate buffer at pH 4 with 0.25 wt% suspensions. The data was processed by Malvern Zetasizer Software v7.13. The zeta potential was calculated as the average of 6 measurements, where each measurement was comprised of 30 to 150

sub-runs.

Semi-contact mode atomic force microscopy (AFM, NTEGRA, NT-MDT, Russia) with Tap300AI-G tips were used for morphology characterization of the CNCs deposited on the silicon wafers (Siegert wafers, Germany). Regions of interest of 5 x 5 $\mu$m were recorded for calculating the dimensions of the CNCs. Significant amounts of potentially single CNC profiles were extracted using the software Gwyddion 2.56 after removing polynomial backgrounds and aligning the rows of the 5 x 5 $\mu$m images. The profiles were baseline corrected using polynomial fitting; the height was calculated from the resulting profile.

### 2.3 Determination of the sulfate half-ester content

Sulfate half-ester content was determined using elemental analysis, XPS and FTIR analyses. The determination of the amount of half-ester groups from the elemental analysis and XPS was performed by fitting the contributions of substituted and unsubstituted AGUs to the experimental data obtained. The monosaccharide compositions considered were AGUs, AGUs with a sulfate half-ester at carbon 6 and 2,3-dialdehyde-AGUs (Figure 1). The fitting searched the minimum molar percentage error for all components analyzed, excluding $Na^+$. For analysis based on XPS data, oxygen, sulfur and carbon were considered.

FTIR data was normalized to 1060 $cm^{-1}$ and the baseline was corrected. The area used for the sulfate was from 770 – 868 $cm^{-1}$ (Gu et al., 2010). The calculated areas were divided by the CNC areas and multiplied by the amount of sulfur (S) detected in the elemental analysis for CNCs.

### 2.4 Determination of the degree of oxidation

The DO during the oxidation reaction was tracked using the periodate consumption by observing UV absorbance at 290 nm (Malaprade, 1928). The reaction of hydroxylamine hydrochloride with the carbonyl groups (Zhao and Heindel, 1991) was used to determine the DO of the products. The DO was determined using an aliquot, containing 0.1 g dry mass of the oxidized CNC derivative and 0.25 M hydroxylamine hydrochloride tuned to pH 4 and stirred for 2.5 hours at room temperature (approx. 20 °C) to ensure to complete the reaction. The solution was titrated back to pH 4 with 0.01 M NaOH using SI Analytics TitroLine 7000. The method is referred to as titration. Elemental analysis was also used for establishing the DO by fitting the contributions of substituted and unsubstituted AGUs to the experimental data obtained.

A method based on solid-state $^{13}C$ CP/MAS NMR was also used (Leguy et al., 2018) in the determination of DO. As a first approximation, it was assumed that the signals of the remaining unmodified cellulose after periodate treatment were the same as in the starting material. Since the C1 signal of cellulose at 104 ppm

is the only region where the spectra of untreated cellulose and fully oxidized cellulose do not overlap, it was used to calculate the DO using the C1 integral of oxidized cellulose ($\int$ C1) relative to the one of the corresponding non-oxidized cellulose ($\int$ $C1_0$). After normalizing the entire spectrum to unity, the C1 integral was calculated from deconvolution. The degree of oxidation determined by NMR spectroscopy ($DO_{NMR}$) is defined by the number of aldehyde groups per glycosyl residue and calculated using in Equation 2.

$$DO_{NMR} = \left(1 - \frac{\int C1}{\int C1_0}\right) \tag{2}$$

## 2.5 Determination of the crystallinity index

WAXS analysis was used to determine the crystallinity index ($CI_{WAXS}$) and the crystallite size of selected CNCs. The diffraction patterns obtained were deconvoluted to Voigt functions using OriginPro (2021). The crystallinity (Equation 4) was calculated using the crystalline area, $A_{crystal}$, and the amorphous area, $A_{amorphous}$, which peak was located approx. 18° 2$\theta$ (Equation 3). The crystalline area was composed by the crystalline areas of the following peaks: (101), (10$\bar{1}$), (021), (002). The crystallite size was determined using the Scherrer equation, using 0.9 as the correction factor (Nam et al., 2016).

$$A_{crystal} = A_{101} + A_{10\bar{1}} + A_{012} + A_{002} \tag{3}$$

$$CI_{WAXS}(\%) = \left(\frac{A_{crystal}}{A_{amorphous} + A_{crystal}}\right) \cdot 100 \tag{4}$$

The CI was also calculated by FTIR, $CI_{FTIR}$, using the method by Siller et al. (2015). The $CI_{FTIR}$ was calculated from the ratio of the peak heights at 1370 over 2900(Nelson and O'Connor, 1964).

In addition to WAXS and FTIR, crystallinity index was also determined by solid-state NMR spectroscopy. Using a deconvolution-based method presented elsewhere (Palme et al., 2014), the informative C4 region was used to obtain CI.

## 2.6 Determination of the degree of surface substitution

The surface ratio ($R_{sur}$) was defined as the ratio between the number of surface cellulose chains, $n_{sur}$, and the total number of cellulose chains of the CNCs. The $R_{sur}$ was calculated using WAXS data and Equation 5, where $d_{(110)}d_{(1\bar{1}0)}$ are the plane spacings, and $L_2$ and $L_1$ are the height and the width of the crystal, respectively (Habibi et al., 2006; Eyley and Thielemans, 2014).

$$R_{sur} = \frac{n_{sur}}{\sum n} = \frac{2\left(\frac{L_1}{d_{(110)}}\right) + 2\left(\frac{L_2}{d_{(1\bar{1}0)}}\right)}{\frac{L_1 L_2}{d_{(110)} d_{(1\bar{1}0)}}} \tag{5}$$

The degree of surface substitution (DSS) of DO, $DSS_{DO}$ (Equation 6), and the sulfate half-ester groups, $DSS_S$ (Equation 7), were determined as being the amount of 2,3-dialdehyde-AGUs, $n_{ox}$ and AGUs with the sulfate half-ester at C6, $n_S$ per surface cellulose chains. The degree of surface sites used, $DSS_U$, was defined as the percentage of the surface modified AGUs and the actual surface of the AGUs that was modifiable (Equation 8). Due to the 180° angle of the $\beta$-1,4-glycosidic linked glucose units, every other superficial AGU was considered modifiable by oxidation while every other superficial AGU was considered able to host an AGU with a sulfate half-ester group. Thus, the $DSS_U$ was calculated as the number of molecules substituted by the surface molecules modifiable by each type of modification. In Equation 7, $c_S$ is the sulfur molar concentration from elemental analysis.

$$DSS_{DO} = \frac{n_{ox}}{n_{sur}} = \frac{DO}{R_{sur}} \tag{6}$$

$$DSS_S = \frac{n_S}{n_{sur}} = \frac{c_S}{R_{sur}} \tag{7}$$

$$DSS_U = \frac{n_{ox}}{\frac{n_{sur}}{2}} + \frac{n_S}{\frac{n_{sur}}{2}} \tag{8}$$

### 2.7 Statistical analysis

The statistical analysis performed in this paper, namely linear fittings, non-linear fittings, descriptive statistics, F-test and ANOVA with the Bonferroni-Holm test, were performed using the software OriginLab Pro (2021). The variations are considered significant at P-values less than 0.05.

## 3 Results and discussion

### 3.1 Oxidation kinetics and composition of the CNCs

According to the elemental analysis (Table 1), a sulfate half-ester group resided in every 18th glucose unit present prior to desulfation, and was reduced to every 69th unit after desulfation. The CNC and the desulfCNCs were subjected to periodate oxidation. The consumption of sodium periodate was monitored *in situ* by determining the UV absorbance (Figure 2), which was fitted to a pseudo first-order kinetic reaction (Liu et al., 2012). The calculated reaction rate of the consumption periodate for the oxidation of CNC was $k_1' = -1.98^{-5} \pm 1{\cdot}10^{-6}$ $s^{-1}$. The reaction rate coefficient for the desulfCNCs was higher: $k_2' = -5.09{\cdot}10^{-5} \pm 4{\cdot}10^{-6}$ $s^{-1}$. Both regressions were considered acceptable according to the R-square. The assumption of a linear dependence on the periodate concentration [P] and the negligible impact of the CNC concentration [AGU] on the rate ($r$) suggested that $r = k[\mathrm{AGU}]^x[\mathrm{P}]^y$, for which $x$ and $y$ are the orders (power dependence of rate on the concentration of the reactant) for each reactant, the order for the AGU was $x << 1$. There is a linear dependence of the rate on the periodate concentration (Figure 2). The reaction rates were statistically different according to the F-test. The decrease in

the content of sulfate half-ester groups on the surface increased the reaction rate coefficient by approx. 150 %. The oxidized CNCs and desulfCNCs are referred to as DAC and desulfDAC, respectively.

Table 1: Elemental analysis of sulfur in the CNCs expressed as wt%. The DO, degree of oxidation is based on periodate consumption determination by UV absorbance. The standard deviation was less than 0.02 wt%.

| Specimen | DO (%) | S (wt%) |
|---|---|---|
| **CNC** | - | 1.09 |
| **DAC** | 12 | 0.71 |
| **DAC** | 29 | 0.69 |
| **DAC** | 57 | 0.66 |
| **desulfCNC** | - | 0.29 |
| **desulfDAC** | 13 | 0.30 |
| **desulfDAC** | 33 | 0.26 |
| **desulfDAC** | 53 | 0.24 |

Periodate oxidation of cellulose with sulfate half-ester groups should result in no change in the sulfur content if the sulfate half-ester groups reside in the C6 position, since they will be unaffected by regioselective oxidation. The decreasing content of S (Table 1) implies that the sulfate groups are, however, affected, and removed, during the oxidation. Where the oxidation of desulfCNC is concerned, the amount decreased slightly and the difference from the first point to the second point was within the standard deviation of the analysis. The O/S ratio (Table S2, Supporting Information) increased for both CNC and desulfCNC when oxidized. In the case where sulfate half-ester groups are not affected, this ratio should not increase with the increasing degree of oxidation. However, the amount of sulfate half-ester groups in the material decreases as the DO of the CNCs increased, regardless of the analysis method used: elemental analysis, FTIR spectroscopy or XPS (Figure 3).

We compared the DO determined by analysis of reactant consumption to the DO values that were determined using titration, solid-state NMR spectroscopy and elemental analysis of the oxidized CNC derivatives (Figure 4). NMR spectroscopy was only performed for the highest DOs used in this study (~50 %). In Figure 5, the $^{13}$C CP/MAS NMR spectra of CNC, desulfCNC, DAC and desulfDAC are shown. The absence of signals in the 160-200 ppm region for DAC and DesulfDAC indicate that there are no aldehyde groups in these materials. This absence can be explained by the fact that the aldehydes have reformed with neighboring hydroxyl groups to provide various hemiacetal and/or hemialdal entities, previously shown to appear as broad peaks in the 90-100 ppm region (Guigo et al., 2014; Azzam et al., 2015; Codou et al., 2015). These newly formed signals overlap with the C1 and C4 signals, and in order to correct for this in the DO calculation, deconvolu-

tion of the affected area was performed (see Supporting Information Table S1 for all parameters). For the CNC and desulfCNC, the number of deconvolution signals were selected according to the native cellulose fibril model, and signals were decomposed into Lorentzian and Gaussian functions for crystalline and amorphous contributions, respectively Heux et al. (1999); Hult et al. (2002). For the DAC and desulfDAC, in addition to the signals above, several Gaussian signals were added to correct for the oxidized material. The deconvolution of this new broad peak area was performed using literature describing oxidized cellulose structures (Plappert et al., 2018; Nypelö et al., 2021), however to fully assign these signals remains a future work. As the C1 signal is consumed during oxidation, the DO could be determined using the Equation 2, and the results obtained were in good agreement with both the titration and the UV absorbance measurements. The DO calculated for the oxidized CNC by elemental analysis was lower compared to the other methods, while the DO calculated by elemental analysis for the desulfCNC was higher than for the other methods employed. This discrepancy could be due to the low accuracy of the method in finding the difference between AGU and dialdehyde-AGU within the elements used for the analysis and the reducing end of cellulose was not taken into account.

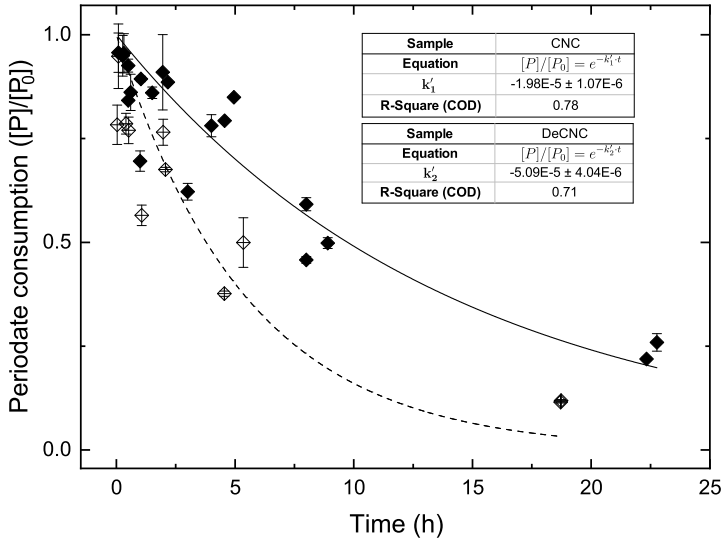


Fig. 2: Consumption of periodate during the oxidation of the CNCs (◆) and desulfCNCs (⊕). The equations containing $k_1'$ and $k_2'$ correspond to CNC and desulfCNC, respectively. R-square, *i.e.*, the coefficient of determination (COD), qualifies the regression. These curves are comprised of three oxidation series for each CNC derivative. Selected points are excluded for clarity but are included in the fitting and statistical analysis.

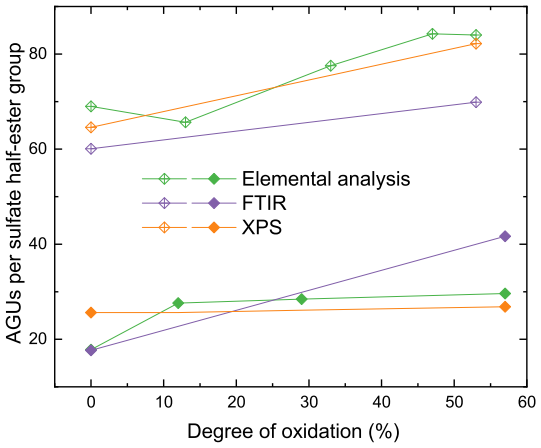


Fig. 3: AGUs per sulfate half-ester groups in CNC and DAC (◆) and desulfCNC and desulfDAC (⊕) with respect to the DO calculated using elemental analysis (green), FTIR area 770-868 $cm^{-1}$ (purple) and XPS analysis (orange).

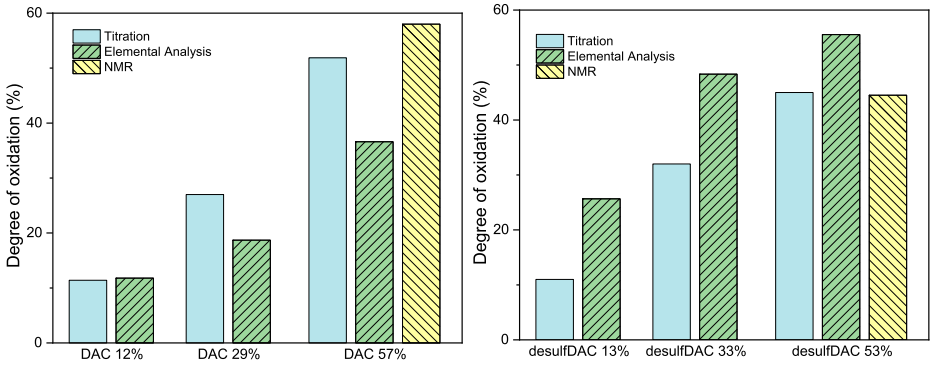


Fig. 4: DO according to titration (cyan), elemental (green) and NMR spectroscopy (yellow) analysis for DACs and desulfDACs.

The sulfate half-esters provide electrostatic repulsion, and hence, colloidal stability. The zeta potential of the CNCs was -28 mV and desulfation increased it to -19 mV (Figure 6). An increase in the DO led to an increase in the zeta potential of both grades. When the DO was approx. 50 %, the zeta potential of both grades was approx. -5 mV and the low zeta potential manifested the colloidal instability.

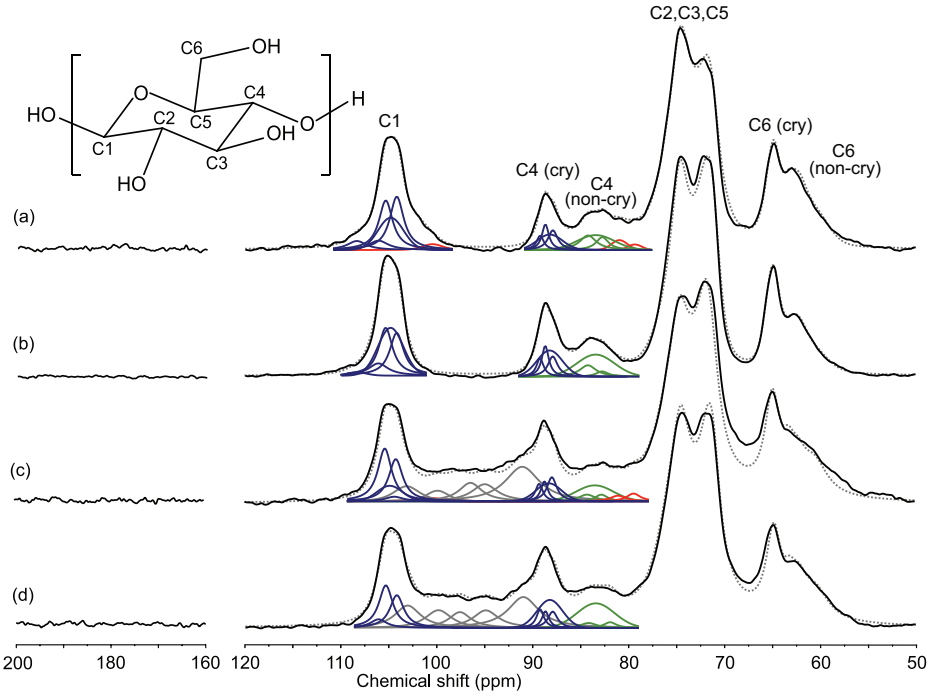


Fig. 5: $^{13}$C CP/MAS NMR spectra of a) CNC, b) desulfCNC, c) DAC, and d) desulfDAC. Deconvoluted signals in the spectrum are attributed to the different cellulose moieties of the cellulose fibril model, with crystalline and paracrystalline signals in blue, non-crystalline accessible fibril surface and inaccessible fibril signals in green, and overlapping cellulose oligomer signals in red. Several broad signals were added, shown in gray, to correct for the oxidized material. The sum of the deconvolution is shown by dotted gray line.

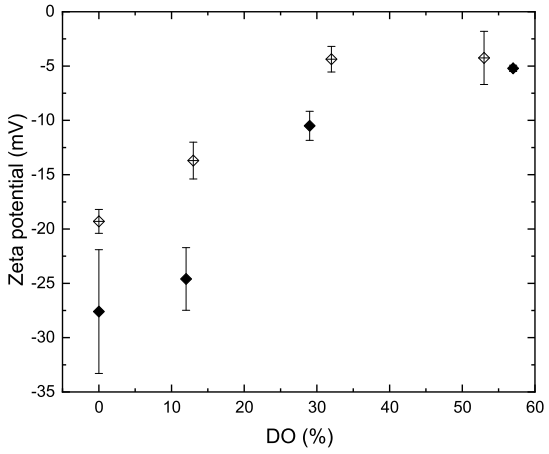


Fig. 6: Zeta potential of CNCs and DACs (◆) and desulfCNCs and desulfDACs (⊕).

### 3.2 CNC dimension

The decrease in the sulfur content of DACs implies that the sulfate half-ester groups were affected by oxidation. We suggest that this decrease in S content was caused either by the cleaving off of the sulfate half-ester groups or by the peeling off of cellulose chains from the surface, which are then removed during purification via dialysis. The diameter of the CNCs and desulfCNCs, 4.1 ± 1.0 and 4.0 ± 1.5 nm, respectively (Figure 7), were statistically not different (Table S3, Supporting information) thereby suggesting that desulfation did not decrease the diameter of the CNC. Oxidation of CNCs into DAC with a DO of 57 % led to a decrease in the diameter down to 3.0 ± 0.8 nm. The average diameters of the CNC and DAC were statistically different, supporting the hypothesis that cellulose chains peel off due to oxidation. The average diameter of desulfDAC, however, increased. The desulfDAC with a DO of 53 % was not statistically different from the non-oxidized grades, hence not supporting the hypothesis of oxidation leading to peeling off of CNC surface chains. We did, however, note that the desulfDAC aggregated in the suspension, as evidenced by the close to neutral zeta potential (Figure 6), and consequently on the silicon support, thereby increasing uncertainty in the determination of diameter.

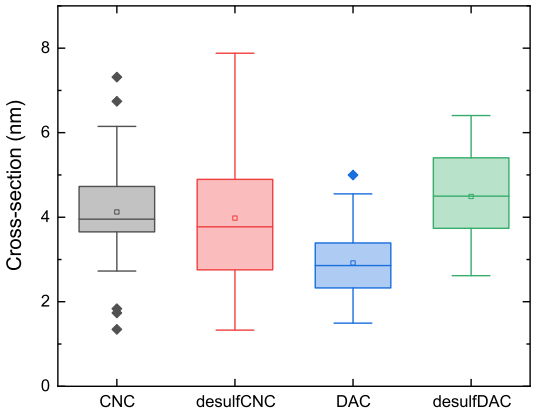


Fig. 7: Dimensions of the CNCs determined using AFM analysis of height profiles. The degree of oxidation of DAC and desulfDAC was 57 % and 53 %, respectively.

### 3.3 Crystallinity

Desulfation, which uses an acid that cleaves the sulfate half-ester groups, resulted in CI increasing in all three methods studied (Figure 8). Besides, cleaving off the

sulfate half-ester groups, the acid appeared to remove regions of less organized polysaccharide chains that led, in turn, to the increase observed in the CI. This is, indeed, directly seen in Figure 5a by the overall NMR spectral sharpening of the desulfCNC compared to CNC, particularly in the C1 (100-113 ppm) and C4 (79-92 ppm) regions. Periodate oxidation has been shown to decrease the CI of cellulose (Liu et al., 2012) and consequently, the CI of oxidized grades decreased compared to the non-oxidized CNC and desulfCNC using WAXS and FTIR (Figure 8). For the DAC and desulfDAC the spectral resolution was too poor to determine the CI using NMR. In general, the $CI_{WAXS}$ was higher than the CI calculated by NMR spectroscopy and FTIR due the inherent methods (Park et al., 2010).

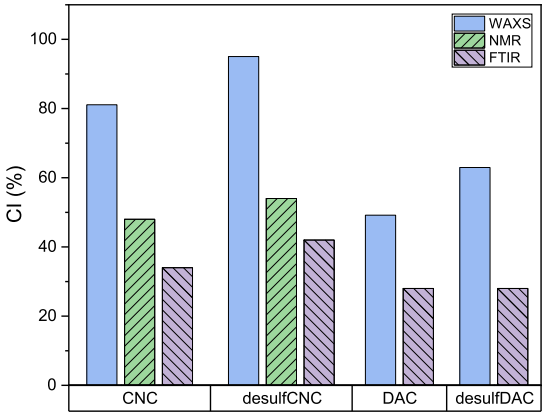


Fig. 8: Crystallinity index of CNC, desulfCNC and their oxidized derivates DAC and desulfDAC in DO 57 % and 53 %, respectively. The CI was determined using wide angle X-ray analysis (blue), NMR spectroscopy (green, only for CNC and desulfCNC) and FTIR (purple).

### 3.4 Degree of surface substitution

The ratio between the cellulose chains present on the surface and the total cellulose chains, $R_{sur}$ (Table 2) decreased with oxidation, which implies a reduction in diameter. The unit cell is considered as remaining unaltered so the smaller the diameter, the larger the fraction of cellulose chains located on the surface. The degree of surface functionality of the CNC derivatives is shown in Table 2. The $DSS_{DO}$ decreased, as expected, with desulfation but also with oxidation due to the S content decreasing (Table 1 and Figure 4), thereby complying with the findings of Lin and Dufresne (2014). At the degree of oxidation in the oxidized grades, the

$DSS_{DO}$ indicated that almost all of the chains present on the surface were oxidized.

The rotation of AGUs due to the glycosidic bond means, however, that not all of the functionalities can be placed on the surface of every cellulose molecule: the substitution present on both oxidized grades, *i.e.*, DAC and desulfDAC, therefore almost doubled the number of sites accessible on the surface for such a degree of modification. The requirement that such a high degree of surface be available suggests that those functionalities were located elsewhere than on the surface, which we suggest were in chains that had been peeled off during oxidation.

Table 2: Distribution of the moieties on the surface of the CNC derivates. S: Number of molecules per each sulfate half-ester group. DO: degree of oxidation from UV absorbance. $R_{sur}$: ratio of molecules on the surface per total molecules. $DSS_S$: degree of surface substitution of S on all the molecules on the surface. $DSS_{DO}$: degree of surface substitution of sulfur on all the molecules on the surface. $DSS_U$: degree of surface sites used to achieve such amounts of moieties on the surface.

| **Sample** | **S** | **DO (%)** | $R_{\mathbf{sur}}$ **(%)** | $\mathbf{DSS_S}$ **(%)** | $\mathbf{DSS_{DO}}$ **(%)** | $\mathbf{DSS_U}$ **(%)** |
|---|---|---|---|---|---|---|
| CNC | 18 | 0 | 38 | 15 | 0 | 30 |
| desulfCNC | 69 | 0 | 38 | 3.8 | 0 | 7.7 |
| DAC | 30 | 57 | 56 | 6.0 | 102 | 215 |
| desulfDAC | 84 | 53 | 53 | 2.2 | 100 | 205 |

## 4 Conclusions

Sulfate half-ester groups are present in most industrially available CNCs, which are moreover often modified for functionality. Oxidation using periodate is a way of oxidizing the cellulose by opening the ring structure, equipping the molecule with aldehyde or alcohol functionality and altering, for example, reactivity and the thermal moldability. However, the role played by sulfate half-ester groups in periodate oxidative modification and its products has not previously been elucidated. The understanding of their impact and function is crucial for further chemical modifications.

We have demonstrated that the sulfate half-ester groups decrease the oxidation reaction rate. Increasing the degree of oxidation led to a decrease in the sulfate half-ester group content independent of its initial content, which was proven not only by a decrease in sulfur content, but also by an increase in the zeta potential. The control of the desulfation by oxidation could lead to a DAC with the

desired colloidal properties. The conclusion we draw is that desulfation is due to the peeling-off of the cellulose chains from the CNC surfaces.

A scenario in which an aldehyde functionality was introduced to the use of CNCs has been examined. In this particular situation, it is necessary that the effect had by the sulfate half-ester groups on the reaction time and conditions is known in order to optimize the reaction. Moreover, improving knowledge of how the sulfate half-ester group content develops (*i.e.*, decreases) with oxidation allows us to contribute to creating materials in which they are desired in varying amounts together with the aldehyde functionality. Lastly, we have made discoveries pertaining to the degradation mechanism of the crystalline cellulose during periodate oxidation via observations of the sulfur content, which we then employed as a direct measurement of the loss of the surface layers on CNCs.

## Declarations

### Conflict of interest

The authors declare that they have no conflict of interest.

### Funding

We are grateful for the financial support of Wallenberg Wood Science Center and the Materials Science Area of Advance at Chalmers.

### Availability of data and material

Not Applicable

### Code availability

Not Applicable

## Supporting information

NMR spectroscopy deconvolution chemical shifts and line widths. Complete elemental analysis. Bonferroni-Holm test comparing the dimensions of the CNC derivatives.

**Acknowledgments**

Anne Wendel and Adrián Rodriguez, at Chalmers University of Technology, are acknowledged for their assistance in making the XPS and WAXS measurements, respectively, and Chalmers Materials Analysis Laboratory (CMAL) for allowing WAXS and XPS to be used. Johan Bergenholtz, at The University of Gothenburg, is thanked for enabling the zeta potential measurements to be made. The NMR measurements were carried out at the Swedish NMR Centre, Gothenburg, Sweden.

**References**

Azzam F, Galliot M, Putaux JL, Heux L, Jean B (2015) Surface peeling of cellulose nanocrystals resulting from periodate oxidation and reductive amination with water-soluble polymers. Cellulose 22(6):3701–3714, DOI 10.1007/s10570-015-0785-x

Codou A, Guigo N, Heux L, Sbirrazzuoli N (2015) Partial periodate oxidation and thermal cross-linking for the processing ofthermosetall-cellulose composites. Composites Science and Technology 117:54–61, DOI 10.1016/j.compscitech.2015.05.022

Conley K, Whitehead MA, van de Ven TG (2017) Probing the structural chirality of crystalline cellulose with induced circular dichroism. Cellulose 24(2):479–486, DOI 10.1007/s10570-016-1130-8

Dash R, Foston M, Ragauskas AJ (2013) Improving the mechanical and thermal properties of gelatin hydrogels cross-linked by cellulose nanowhiskers. Carbohydrate Polymers 91(2):638–645, DOI 10.1016/j.carbpol.2012.08.080

Eyley S, Thielemans W (2014) Surface modification of cellulose nanocrystals. Nanoscale 6(14):7764–7779, DOI 10.1039/C4NR01756K

Gu J, Catchmark JM, Archibald DD, Kaiser EQ (2010) Determination of sulfate esterification levels in cellulose nanocrystals by attenuated total reflectance - Fourier transform infrared spectroscopy. American Society of Agricultural and Biological Engineers Annual International Meeting 2010, ASABE 2010 1(10):23–32, DOI 10.13031/2013.29598

Guigo N, Mazeau K, Putaux JL, Heux L (2014) Surface modification of cellulose microfibrils by periodate oxidation and subsequent reductive amination with benzylamine: a topochemical study. Cellulose 21(6):4119–4133, DOI 10.1007/s10570-014-0459-0

Habibi Y, Chanzy H, Vignon MR (2006) TEMPO-mediated surface oxidation of cellulose whiskers. Cellulose 13(6):679–687, DOI 10.1007/s10570-006-9075-y

Heux L, Dinand E, Vignon M (1999) Structural aspects in ultrathin cellulose microfibrils followed by 13C CP-MAS NMR. Carbohydrate Polymers 40(2):115–124, DOI 10.1016/S0144-8617(99)00051-X

Hult EL, Larsson PT, Iversen T (2002) A Comparative CP/MAS 13C-NMR Study of the Supermolecular Structure of Polysaccharides in Sulphite and Kraft Pulps. Holzforschung 56(2):179–184, DOI 10.1515/HF.2002.030

Jordan JH, Easson MW, Condon BD (2019) Alkali Hydrolysis of Sulfated Cellulose Nanocrystals: Optimization of Reaction Conditions and Tailored Surface Charge. Nanomaterials 9(9):1232, DOI 10.3390/nano9091232

Kim UJ, Kuga S, Wada M, Okano T, Kondo T (2000) Periodate oxidation of crystalline cellulose. Biomacromolecules 1(3):488–492, DOI 10.1021/bm0000337

Kontturi E, Laaksonen P, Linder MB, Nonappa, Gröschel AH, Rojas OJ, Ikkala O (2018) Advanced materials through assembly of nanocelluloses. Advanced Materials 30(24):1703,779, DOI 10.1002/adma.201703779

Koso T, Rico del Cerro D, Heikkinen S, Nypelö T, Buffiere J, Perea-Buceta JE, Potthast A, Rosenau T, Heikkinen H, Maaheimo H, Isogai A, Kilpeläinen I, King AWT (2020) 2D Assignment and quantitative analysis of cellulose and oxidized celluloses using solution-state NMR spectroscopy. Cellulose 27(14):7929–7953, DOI 10.1007/s10570-020-03317-0

Larsson PA, Berglund LA, Wågberg L (2014) Highly ductile fibres and sheets by core-shell structuring of the cellulose nanofibrils. Cellulose 21(1):323–333, DOI 10.1007/s10570-013-0099-9

Leguy J, Nishiyama Y, Jean B, Heux L (2018) Ultrastructural characterization of the core–shell structure of a wide range of periodate-oxidized cellulose from different native sources by solid-state $^{13}$C CP-MAS NMR. ACS Sustainable Chemistry & Engineering 7(1):412–420, DOI 10.1021/acssuschemeng.8b03772

Liimatainen H, Visanko M, Sirviö JA, Hormi OE, Niinimaki J (2012) Enhancement of the nanofibrillation of wood cellulose through sequential periodate-chlorite oxidation. Biomacromolecules 13(5):1592–1597, DOI 10.1021/bm300319m

Lin N, Dufresne A (2014) Surface chemistry, morphological analysis and properties of cellulose nanocrystals with gradiented sulfation degrees. Nanoscale 6(10):5384–5393, DOI 10.1039/C3NR06761K

Liu X, Wang L, Song X, Song H, Zhao JR, Wang S (2012) A kinetic model for oxidative degradation of bagasse pulp fiber by sodium periodate. Carbohydrate Polymers 90:218–223, DOI 10.1016/j.carbpol.2012.05.027

López Durán V, Larsson PA, Wågberg L (2018) Chemical modification of cellulose-rich fibres to clarify the influence of the chemical structure on the physical and mechanical properties of cellulose fibres and thereof made sheets. Carbohydrate Polymers 182:1–7, DOI 10.1016/j.carbpol.2017.11.006

Malaprade L (1928) Oxidation of some polyalcohols by periodic acid—applications. Comptes Rendus 186:382–384

Nam S, French AD, Condon BD, Concha M (2016) Segal crystallinity index revisited by the simulation of X-ray diffraction patterns of cotton cellulose I$\beta$ and cellulose II. Carbohydrate Polymers 135:1–9, DOI 10.1016/j.carbpol.2015.08.035

Nelson ML, O'Connor RT (1964) Relation of certain infrared bands to cellulose crystallinity and crystal lattice type. Part II. A new infrared ratio for estimation of crystallinity in celluloses I and II. Journal of Applied Polymer Science 8(3):1325–1341, DOI 10.1002/app.1964.070080323

Nypelö T, Amer H, Konnerth J, Potthast A, Rosenau T (2018) Self-Standing Nanocellulose Janus-Type Films with Aldehyde and Carboxyl Functionalities. Biomacromolecules 19(3):973–979, DOI 10.1021/acs.biomac.7b01751

Nypelö T, Berke B, Spirk S, Sirviö JA (2021) Review: Periodate oxidation of wood polysaccharides—Modulation of hierarchies. Carbohydrate Polymers 252:117,105, DOI 10.1016/j.carbpol.2020.117105

Palme A, Idström A, Nordstierna L, Brelid H (2014) Chemical and ultrastructural changes in cotton cellulose induced by laundering and textile use. Cellulose 21(6):4681–4691, DOI 10.1007/s10570-014-0434-9

Park S, Baker JO, Himmel ME, Parilla PA, Johnson DK (2010) Cellulose crystallinity index: measurement techniques and their impact on interpreting cellulase performance. Biotechnology for Biofuels 3(1):10, DOI 10.1186/1754-6834-3-10

Plappert SF, Quraishi S, Pircher N, Mikkonen KS, Veigel S, Klinger KM, Potthast A, Rosenau T, Liebner FW (2018) Transparent, Flexible, and Strong 2,3-Dialdehyde Cellulose Films with High Oxygen Barrier Properties. Biomacromolecules 19(7):2969–2978, DOI 10.1021/acs.biomac.8b00536

Potthast A, Kostic M, Schiehser S, Kosma P, Rosenau T (2007) Studies on oxidative modifications of cellulose in the periodate system: Molecular weight distribution and carbonyl group profiles. Holzforschung 61(6):662–667, DOI 10.1515/HF.2007.099

Potthast A, Schiehser S, Rosenau T, Kostic M (2009) Oxidative modifications of cellulose in the periodate system - Reduction and beta-elimination reactions: 2nd ICC 2007, Tokyo, Japan, October 25-29, 2007. Holzforschung 63(1):12–17, DOI 10.1515/HF.2009.108

Siller M, Amer H, Bacher M, Roggenstein W, Rosenau T, Potthast A (2015) Effects of periodate oxidation on cellulose polymorphs. Cellulose 22(4):2245–2261, DOI 10.1007/s10570-015-0648-5

Sinha A, Martin EM, Lim KT, Carrier DJ, Han H, Zharov VP, Kim JW (2015) Cellulose Nanocrystals as Advanced "Green" Materials for Biological and Biomedical Engineering. Journal of Biosystems Engineering 40(4):373–393, DOI 10.5307/JBE.2015.40.4.373

Sulaeva I, Klinger KM, Amer H, Henniges U, Rosenau T, Potthast A (2015) Determination of molar mass distributions of highly oxidized dialdehyde cellulose by size exclusion chromatography and asymmetric flow field-flow fractionation. Cellulose 22(6):3569–3581, DOI 10.1007/s10570-015-0769-x

Sun B, Hou Q, Liu Z, Ni Y (2015) Sodium periodate oxidation of cellulose nanocrystal and its application as a paper wet strength additive. Cellulose 22(2):1135–1146, DOI 10.1007/s10570-015-0575-5

Vanderfleet OM, Cranston ED (2021) Production routes to tailor the performance of cellulose nanocrystals. Nature Reviews Materials 6(2):124–144, DOI 10.1038/s41578-020-00239-y

Yuldoshov S, Atakhanov A, Rashidova S (2016) Cotton cellulose, microcrystalline cellulose and nanocellulose: Carboxymethylation and oxidation reaction activity. Journal of Nanoscience and Nanotechnology 10(6):106

Zhao H, Heindel ND (1991) Determination of Degree of Substitution of Formyl Groups in Polyaldehyde Dextran by the Hydroxylamine Hydrochloride Method. Pharmaceutical Research 8:400–402, DOI 10.1023/A:1015866104055

Zoppe JO, Larsson PA, Cusola O (2020) Surface modification of nanocellulosics and functionalities. In: Lignocellulosics, Elsevier, pp 17–63

## Supporting Information file for

# The effect of sulfate half-ester groups on cellulose nanocrystal periodate oxidation

**Saül Llàcer Navarro · Koyuru Nakayama · Alexander Idström · Lars Evenäs · Anna Ström · Tiina Nypelö***

S. Llàcer Navarro, K. Nakayama, A. Idström, L. Evenäs, A. Ström, T. Nypelö
Department of Chemistry and Chemical Engineering, Chalmers University of Technology, 41296 Gothenburg, Sweden

S. Llàcer Navarro, K. Nakayama, L. Evenäs, T. Nypelö
WallenbergWood Science Center, Chalmers University of Technology, 41296 Gothenburg, Sweden

*Corresponding author email: tiina.nypelo@chalmers.se

### Nuclear Magnetic Resonance Spectroscopy

Table S1. Results of spectral fitting for the C1, C4 and oxidized compounds region of CP/MAS $^{13}C$ NMR spectrum of cellulose (*cf.* Figure 5).

| | Assignment | d (ppm) | FWHM (Hz) |
|---|---|---|---|
| C1 | Crystalline | 108.4 | 243 |
| | Crystalline | 106.1 | 248 |
| | Crystalline | 105.3 | 175 |
| | Crystalline | 104.8 | 316 |
| | Crystalline | 104.2 | 177 |
| | Non-Crystalline | 102.1 | 255 |
| | Cellulose oligomer | 100.5 | 255 |
| | Oxidized compounds | 103.1 | 323 |
| | Oxidized compounds | 99.8 | 273 |
| | Oxidized compounds | 97.6 | 307 |
| | Oxidized compounds | 94.9 | 321 |
| | Oxidized compounds | 91.0 | 429 |
| C4 | Crystalline | 89.2 | 91 |
| | Crystalline | 88.7 | 87 |
| | Crystalline | 88.2 | 316 |
| | Crystalline | 87.9 | 122 |
| | Amorphous | 84.2 | 209 |
| | Amorphous | 83.4 | 464 |
| | Amorphous | 82.7 | 159 |
| | Cellulose oligomer | 80.9 | 198 |
| | Cellulose oligomer | 79.3 | 174 |

**Elemental analysis**

The sodium content of the CNCs was higher previous to oxidation than the sulfur content indicating that not all sulfate half-ester groups were in $Na^+$ form. The Na/S ratio increased with desulfation indicating that the use of the sodium periodate facilitated a cation exchange of the remaining sulfate groups. However, it could also be a result of decreasing sulfate group content or that the oxidation results in other functionalities than aldehydes only.

Table S2. Elemental analysis of CNCs with various degree of oxidation (DO) expressed as wt%. The standard deviation was less than 0.02 in all cases.

| Derivate | S | H | O | Na | Na/S | O/S |
|---|---|---|---|---|---|---|
| **CNC** | 1.09 | 5.60 | 52.20 | 0.39 | 0.35 | 48.11 |
| **DAC DO 11%** | 0.71 | 5.92 | | | | |
| **DAC DO 27%** | 0.69 | 5.85 | | | | |
| **DAC DO 52%** | 0.66 | 5.65 | 54.78 | 0.51 | 0.77 | 82.99 |
| **desulfCNC** | 0.29 | 6.04 | 52.42 | | | 183.93 |
| **desulfDAC DO 11%** | 0.30 | 5.85 | | | | |
| **desulfDAC DO 32%** | 0.26 | 5.60 | | | | |
| **desulfDAC DO 48%** | 0.24 | 5.79 | 53.84 | | | 229.09 |

Table S3 Bonferroni-Holm test comparing the dimensions of the CNC derivatives. Each row represents a comparison between derivate 1 and derivate 2. The p-value and the corrected alpha (rejection criteria) for each individual hypotheses to avoid family-wise error are included. If the p-value is smaller than the corrected alpha the difference is statistically significant.

| Derivate 1 | Derivate 2 | p-value | Alpha | Difference |
|---|---|---|---|---|
| **CNC** | **DAC** | 2.79E-10 | 0.01 | YES |
| **CNC** | **desulfCNC** | 0.42 | 0.05 | NO |
| **desulfCNC** | **desulfDAC** | 0.02 | 0.02 | NO |
| **DAC** | **desulfDAC** | 1.07E-11 | 0.01 | YES |
| **CNC** | **desulfDAC** | 0.10 | 0.03 | NO |
| **DAC** | **desulfCNC** | 1.55E-8 | 0.01 | YES |

# Paper II

**Fat tissue equivalent phantoms for microwave applications by reinforcing gelatin with nanocellulose.**

Hana Dobšíček Trefná, Saül Llàcer Navarro, Fredrik Lorentzon, Tiina Nypelö and Anna Ström.

*Submitted*

# Fat tissue equivalent phantoms for microwave applications by reinforcing gelatin with nanocellulose

**Hana Dobšíček Trefná[1], Saül Llàcer Navarro[2,3], Fredrik Lorentzon[1,2], Tiina Nypelö[2,3] and Anna Ström[2]**

[1]Signal Processing and Biomedical engineering, Department of Electrical Engineering, Chalmers University of Technology, Sweden.
[2]Applied Chemistry, Department of Chemistry and Chemical Engineering, Chalmers University of Technology, Sweden.
[3]Wallenberg Wood Science Center, Chalmers University of Technology, Gothenburg, Sweden.

E-mail: anna.strom@chalmers.se

Received xxxxxx
Accepted for publication xxxxxx
Published xxxxxx

## Abstract

Tissue mimicking phantom materials with thermal and dielectric equivalence are vital for the development of microwave diagnostics and treatment. The current phantoms representing fat tissue are challenged by mechanical integrity at relevant temperatures coupled with complex production protocols. We have employed two types of nanocellulose (cellulose nanocrystals and oxidized cellulose nanocrystals) as reinforcement in gelatin stabilized emulsions for mimicking fat tissue. The water oil ratio being 30:70. The nanocellulose-gelatin stabilized emulsions were evaluated for their dielectric properties, the moduli-temperature dependence using small deformation rheology, stress-strain behavior using large deformation, and their compliance to quality assurance guidelines for superficial hyperthermia. All emulsions had low permittivity and conductivity within the lower microwave frequency band, accompanied by fat equivalent thermal properties. Small deformation rheology showed reduced temperature dependence of the moduli upon addition of nanocellulose, independent of type. The cellulose nano crystals – gelatin reinforced emulsion complied with the quality assurance guidelines. Hence, we demonstrate that the addition of cellulose nanocrystals to gelatin stabilized emulsions have potential to be used as fat phantoms for development of microwave diagnostics and treatment.

Keywords: tissue-mimicking phantom, microwave diagnostics, hyperthermia, emulsion, gel, rheology

---

## 1. Introduction

Microwave applications for medical diagnostics and treatment are emerging in today's health care systems. Microwave devices have advantages of being cost-effective, compact, and portable while providing fast acquisition. The high contrast between dielectric properties of healthy and malignant tissues compensate for mediocre spatial resolution so that the microwave systems can serve as a fast decision tool for diagnostics of stroke and traumas (Fhager *et al.*, 2018; Persson *et al.*, 2014), detection of breast cancer (Poplack *et al.*, 2007; Meaney *et al.*, 2013; Porter *et al.*, 2015; Fear *et al.*, 2013) or localization of epileptic brain activity (Eadie, 2016). Another application of microwaves is hyperthermia cancer treatment, in which the tumor temperature is elevated to therapeutic levels to kill the tumor cells and/or making them vulnerable to other treatment modalities, such as radiotherapy and chemotherapy (Datta *et al.*, 2015; Cihoric *et al.*, 2015; Paulides *et al.*, 2020; Issels *et al.*, 2018).

Development and verification of both the diagnostic and treatment systems require tissue-mimicking phantoms. A phantom is a physical structure made from materials that together imitate the characteristics of the biological tissue in terms of either electromagnetic (EM) wave propagation, thermal redistribution of heat, or both. Microwave diagnostics is based on differentiating dielectric properties of tissue and therefore demand phantoms that model the electrical conductivity and permittivity of the tissue with high accuracy. Hyperthermia phantoms have an additional demand of thermal equivalence to enable accurate measurements of power and temperature deposition patterns of the applicators (Trefná *et al.*, 2017; Dobšíček Trefná *et al.*, 2019).

The phantoms are standardly divided into two classes, representing either high water content tissues, such as muscle, brain or tumor, that have values of permittivity ($\varepsilon_r$) between 40-80 and electrical conductivity ($\sigma$) between 0.4 – 1 S/m (Hasgall PA *et al.*, 2018) or the low water content tissues, such as fat or bone, that have values of $\varepsilon_r$ between 6 and 25 and values of $\sigma$ between 0.05 – 0.4 S/m in frequency range of 100 MHz – 1GHz. Different compositions of phantoms mimicking muscle, brain, skin and tumor have been proposed based on hydrophilic gel formers such as agar-agar or carrageenan (Duan *et al.*, 2014; Ito *et al.*, 2001; Kato and Ishida, 1987; Fontes-Candia *et al.*, 2021) polyacrylamide (Bini *et al.*, 1984; Kato *et al.*, 1986), or gelatin (Lazebnik *et al.*, 2005; Madsen *et al.*, 1982; Yuan *et al.*, 2012). However, non-toxic, self-standing, easy to prepare phantoms to represent the low water content tissues characterized by low $\varepsilon_r$ is lacking. Numerous dry phantoms have been introduced in the past, their complicated preparation procedures and often poor reproducibility have hampered their use. Acetylene black mixed with aluminum powder and laminac polyester resin (Allen *et al.*, 1988) carbon doped paraffin solution dispersed in silicone rubber (Nikawa *et al.*, 1996) and graphite powder and urethane rubber (Garrett and Fear, 2014) are examples of currently available phantoms. Alternative to dry phantoms is the use of water dispersions of glycerin or nonionic surfactant Triton-X to tune permittivity for complex breast phantoms (Joachimowicz *et al.*, 2014). The liquids are poured into 3D printed containers derived from magnetic resonance imaging. However, often the thermal equivalence required for hyperthermia is not met, and the phantoms are neither self-standing or cuttable and the plastic containers can distract the EM field propagation on the boundary between the liquid and plastic, thus challenging the diagnostics (Rydholm *et al.*, 2017).

The oil-in-water emulsion phantom that utilizes gelatin as a solidifier has the potential to overcome most of the current challenges (Lazebnik *et al.*, 2005; Madsen *et al.*, 1982). Gelatin forms a random coil conformation in hot water, upon cooling it forms a self-standing gel through the formation of rigid triple helices connected by flexible links (Parker and Povey, 2012; Hellio and Djabourov, 2006). The shear modulus and the strength of the resulting gel is defined by the concentration of triple helices (Hellio and Djabourov, 2006). Gelatin is used in a vast range of applications from food to pharma (van Vlierberghe *et al.*, 2011) and is hence readily available. The temperature, at which the solution to gel (sol-gel) transition occurs is typically between 25-35 °C and it is independent of gelatin concentration (Simon *et al.*, 2003; Tosh and Marangoni, 2004). The sol-gel transition of gelatin is reversible, albeit with hysteresis (Djabourov and Papon, 1983). The low melting temperature and other limitations accompanied with current phantom recipes, such as development of air bubbles during preparation, complicated preparation procedures and use of toxic aldehydes as crosslinking agents hamper the successful implementation of this gelatin-based phantoms in quality assurance (QA) (Trefná *et al.*, 2017; Dobšíček Trefná *et al.*, 2019) and other verification procedures.

Cellulose materials are widely used in engineered and pharmaceutical products such as in paper and tablets. The establishment of cellulose nanomaterials has furthermore expanded the use of cellulose as viscosity modifiers and to reinforce composite materials (Dufresne, 2012). Cellulose particles have been demonstrated to provide strength to gelatin networks (Wang *et al.*, 2017). Of specific interest have been the nanosized cellulose particles that can be dispersed in a hydrophilic environment such as water (Mondragon *et al.*, 2015). Further surface modification of the nanosized celluloses have been shown to enable a chemical linkage between gelatin and the cellulose, creating covalent reinforcement of the network. The specifically demonstrated modification has involved oxidation of cellulose hydroxyl groups into carbonyl groups that can form a covalent imine bond with amine groups of lysine in gelatin (Kwak *et al.*, 2020; Dash *et al.*, 2013).

In this work, we have utilized emulsions, kinetically stabilized by gelatin and nanocellulose to prepare self-standing phantoms with the dielectric and thermal properties of low water content tissues. Three different phantoms were developed; emulsions stabilized by gelatin, emulsion stabilized by gelatin and cellulose nanocrystals (CNC) and emulsion stabilized by gelatin and dialdehyde CNC, hereafter referred to as DAC. We have demonstrated that all developed fat mimicking phantoms fulfill requirements of dielectric and mechanical properties. In addition, the nanocellulose enforced the thermal integrity of the phantoms, increasing the temperature range at which the phantom can be used.

## 2. Material and Methods

### *2.1 Materials*

Cellulose nanocrystals (CNCs) were purchased from Celluforce (Canada). Gelatin was kindly provided by Gelita, Sweden, Bloom 296 Gelatin A. Solec lecithin B-10 was kindly provided by Dupont, Denmark. Sodium periodate and hydroxylamine were purchased from Merck, Sweden. Rapeseed oil was a commercial grade purchased from local supermarket (Coop X-tra brand), Sweden. Milli-Q water was used throughout the study with resistivity of 18.2 $\Omega^{-1}$ $cm^{-1}$ at 25 ºC.

### *2.2 Methods*

*CNC dispersion:* CNCs were dispersed in Milli-Q water at 3.5 wt% concentration. The dispersion was mixed with a magnetic stirrer during addition of CNCs into water, followed by horizontal shaking at room temperature overnight. The dispersion was ultrasonicated for 15 minutes (VWR USC900D), ensuring that the temperature did not increase above 40 °C.

*Production of dialdehyde CNCs through oxidation (DAC):* The oxidation of CNCs was performed according to Dash *et al.* (2013) using a weight ratio of sodium periodate to CNC of 0.7. The reaction time was 6 hours and reaction vessel was covered with aluminum foil. The reaction was quenched by addition of glycerol, after which it was dialyzed in water for two days using membranes with 12-14 000 g/mol cutoff. The solid content of the dialyzed dispersion was 3 wt%. The dispersion was stored at 4 ºC until further use.

*Preparation of gelatin stabilized emulsions:* The oil and water were heated separately to 60 °C. Lecithin was dispersed in the hot water and left to mix for 10 minutes, after which the gelatin. Gelatin was let to dissolve for 20 minutes. Oil was then added dropwise to the gelatin-water system under vigorous stirring using Ultra-turrax (IKA T50) resulting in visually turbid system. The system was poured into molds and cooled to 20 °C. The size of the molds used for preparing emulsions for mechanical testing were 10 mm in diameter and height, and for analysis of dielectric properties 100 mm in diameter. The emulsions were kept refrigerated until further use. See Table 1 for final compositions of emulsions used in this study.

*Preparation of CNC/DAC-gelatin stabilized emulsions:* The emulsions were prepared similar to the gelatin emulsions except that the CNC or DAC dispersion were heated to 50 °C, added to the gelatin-water system and further incorporated with the oil. Note that the gelatin solution has to be of a high concentration as the system is diluted by the water dispersion of CNC and DAC. See Table 1 for final compositions of emulsions used in this study.

*Confocal Laser scanning microscopy (CLSM)* was used for visualization of the emulsion structure using Nikon Ti-E/A1+ microscope.

*Differential Scanning Calorimetry (DSC)*: Heat capacities were determined using Mettler-Toledo, model DSC 2. STARe software was used for calculating the specific heat using the average of the range of 15° C to 45° C in a heating ramp of 10 K/min. Medium pressure crucibles of 7 mm diameter (ME-29990) were used.

**Table 1:** Final compositions of the gelatin and CNC/DAC-gelatin stabilized emulsions. All concentrations are given in wt%, based on the total weight of the final emulsion.

| Sample Name | Water | Oil | Lecithin | Gelatin | CNC | DAC |
|---|---|---|---|---|---|---|
| Gelatin stabilized emulsion | 27.4 | 70 | 0.6 | 2 | | |
| CNC-gelatin stabilized emulsion | 26.8 | 70 | 0.6 | 2 | 0.6 | |
| DAC-gelatin stabilized emulsion | 26.8 | 70 | 0.6 | 2 | | 0.6 |

*Rheology:* The rheological properties of the emulsions were determined using a DHR-3 rheometer from TA Instruments, Denmark. The geometry used was plate-plate (40 mm in diameter) with a gap of 1 mm. The upper plate was equipped with a solvent trap and used with a custom-made evaporation chamber from TA Instruments. The samples were added to the plate at 60 ºC, the upper plate was lowered to measurement position and the temperature was reduced to 10 °C with a rate of 2 °C $min^{-1}$. The storage (G') and loss (G") modulus of the samples were recorded at a frequency of 1 Hz and a strain of 0.5 %. The temperature was controlled with a Peltier plate.

*Dielectric properties:* The dielectric properties were measured by an open-ended coaxial dielectric probe (85070E, Dielectric Probe Kit DAK 12 (SPEAG, Switzerland) connected to a vector network analyzer (VNA) (Keysight FieldFox, Keysight, USA). The application operation frequency range is 10 MHz to 3 GHz with sweep of 101 points. The dielectric properties of each sample are given as an average of 10 replications. The dielectric properties of the Milli-Q water were measured before and after each sample and then compared to the theoretical dielectric relaxation of water calculated by the Debye process. The difference was applied as calibration for the measurements.

*Mechanical properties:* Mechanical properties of the gels were determined using a texture analyzer TA-HDi from Stable Microsystems, UK. The tests were carried out at room temperature. Gels for stress-strain testing were prepared by pouring the hot dispersion into molds of 10 mm in diameter and 10 mm in height. Stress-strain curves were determined at a crosshead speed of 2 mm/s. The crosshead had a diameter of 20 mm. Free expansion of the gels was assured in the radial direction. True stress ($\sigma_t$) and true strain ($\varepsilon_t$) were calculated using equation 1 and 2:

$$\sigma_t = \frac{F\left(\frac{L}{L_0}\right)}{A_0} \quad \text{eq: 1}$$

$$\varepsilon_t = log\left(\frac{L}{L_0}\right) \quad \text{eq: 2}$$

Where $L$ and $L_o$ is the height and the initial height of the gels, respectively, $A_0$ is the initial cross-section area and $F$ is the force.

*Testing for compliance with QA guidelines for superficial hyperthermia:* Figure 1 shows a schematic representation and a photograph of the setup used for evaluation of the performance of fat phantoms during the hyperthermia QA procedure. The composition follows the QA applicator verification arrangement for superficial hyperthermia as described in (Trefná *et al.*, 2017; Dobšíček Trefná *et al.*, 2019).

In the arrangement (Figure 1), a self-grounded antenna (Takook *et al.*, 2017) was centered on top of a 15 mm thick hydrogel bolus (Trefna and Ström, 2019) placed on top of the multilayered phantom. The applicator has a surface area with diameter 60 mm and water temperature inside the enclosure was kept constant at 20 ºC by circulation. The reflection coefficient of the antenna at frequency 485 MHz was -14.7 dB. The power of 60-63 W was applied for 6 minutes. The hydrogel bolus (Trefna and Ström, 2019) was used ensuring both an optimal contact area with the phantom and extension beyond the radiating aperture. The hydrogel bolus (400x210x15mm$^3$) was placed on top of the multilayered phantom consisting of a 70 mm high muscle-equivalent phantom, upon which two 5 mm fat phantoms of the same area as the muscle phantom were placed. The muscle phantom (380x250x70mm$^3$) was composed of water, sugar, salt and agarose (Duan *et al.*, 2014). The $\varepsilon_r$ of the muscle phantom and hydrogel bolus was 59.2 and 81, respectively. The $\sigma$ for the muscle phantom and the hydrogel bolus was 0.71 S/m and 0.12 S/m, respectively. The phantom and bolus were at room temperature at the start of experiments and their temperatures were not regulated during the heating.

The temperature during the experiments was captured by fiber optic probes (THR-NS-882X, FISO Technologies Inc, Canada) located at three different depths in the center of the central plane of the antenna: at interface between a) bolus and fat phantom (HF), b) fat and muscle phantom (FM), c) at 1 cm depth in the muscle phantom (M1-M3). The three probes located in the muscle phantom contained multiple sensors spaced 10 mm from each other. The temperature distribution in the horizontal plane at top layer of the fat phantom was captured by an infrared camera (B355, FLIR Systems, USA).

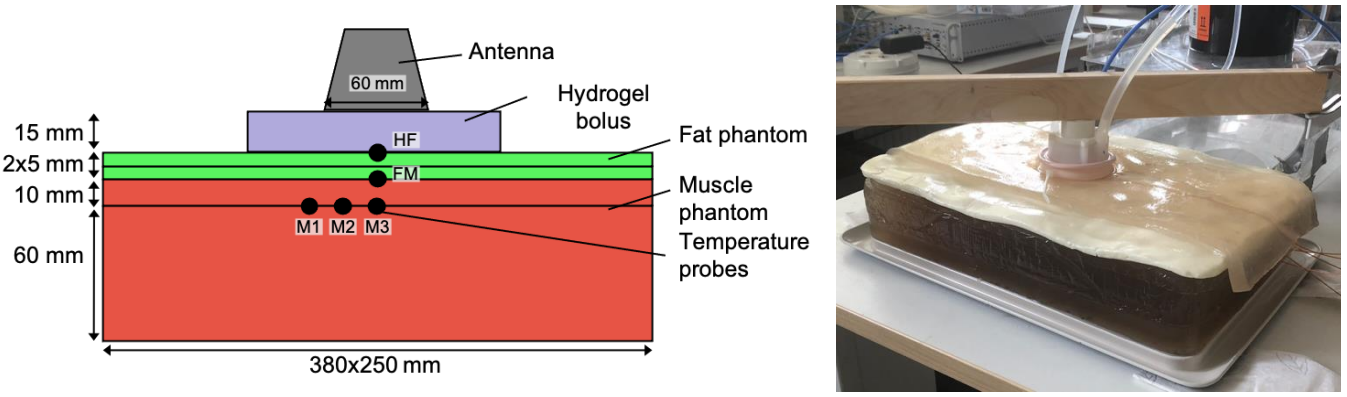


**Figure 1.** Schematic illustration (to the left) and photograph of the hyperthermia QA procedure (to the right). The different parts used, their dimensions and the location of temperature probes are shown in the illustration.

## 3. Results

*3.1 Dielectric properties and heat capacity:* Prediction of dielectric properties of mixtures is complex (Sihvola, 1999) following modified mixing rule principles. Figure 2a illustrates the prediction of permittivity as a function of oil content. Maxwell-Garnett effective medium approximation is valid at low volume fractions of oil, assuming that the domains are spatially, and via interactions, separated (Markel, 2016). Bruggeman approximation excludes the effect of symmetry via volume fraction utilization, however, has limitations above the percolation threshold. The semi-empirical Lichtenecker's logarithmic mixture formula, which has proven to be useful practical formulation for determining the effective permittivity of homogenized dielectric mixtures (Simpkin, 2010), provides a similar prediction of permittivity at high oil fractions, as Bruggeman. Thus, Maxwell-Garnett and Lichtenecker approximations act as a lower and upper bound for the permittivity establishment, indicating 0.7 being the lowest oil fraction required to reach low permittivity's ($\varepsilon_r$ <15). We have therefore focused this study on compositions with oil concentration of 70%. The compositions used (Table 1) led to structures where the oil is enclosed in droplets in the gelatin matrix (Figure 2b).

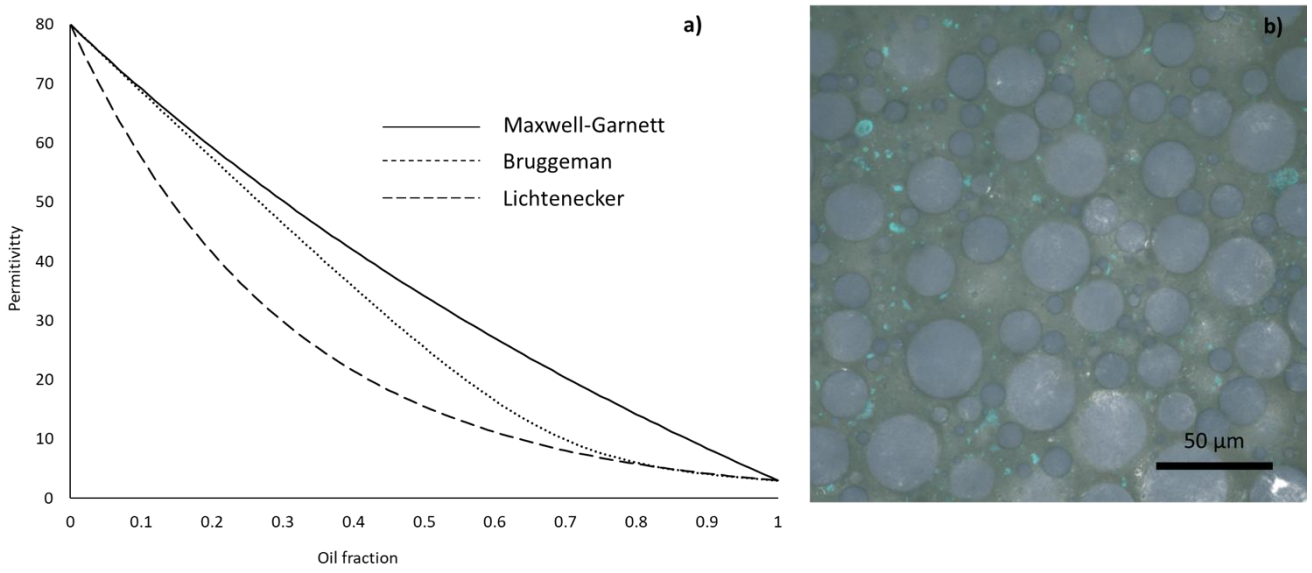


**Figure 2.** Prediction of emulsion permittivity as a function of oil fraction according to Maxwell-Garnett, Bruggeman and Lichtenecker approximations a) and CLSM visualization of a 70/30 gelatin stabilized oil emulsion where oil droplets are enclosed in gelatin matrix b).

The dielectric properties over the frequency range of 0.1 – 3 GHz of the emulsions presented in Table 1 represent the mean values with the confidence interval from 10 different locations (Figure 3). All emulsion exhibited permittivity of ~7-14.5, agreeing well with predictions. In addition, they exhibit low conductivity, hence complying to the dielectric requirements of a fat phantom. The gelatin stabilized emulsion is of highest permittivity with values decreasing from ~14.5 at 10 MHz to above 12 at 3 GHz. The CNC-gelatin reinforced phantom exhibited permittivity between 7 and 9. The permittivity values obtained lay within the bounds of Maxwell-Garnett and Lichtenecker. Specific heat of the emulsions were $C_p$ 3218 J/(kg C).

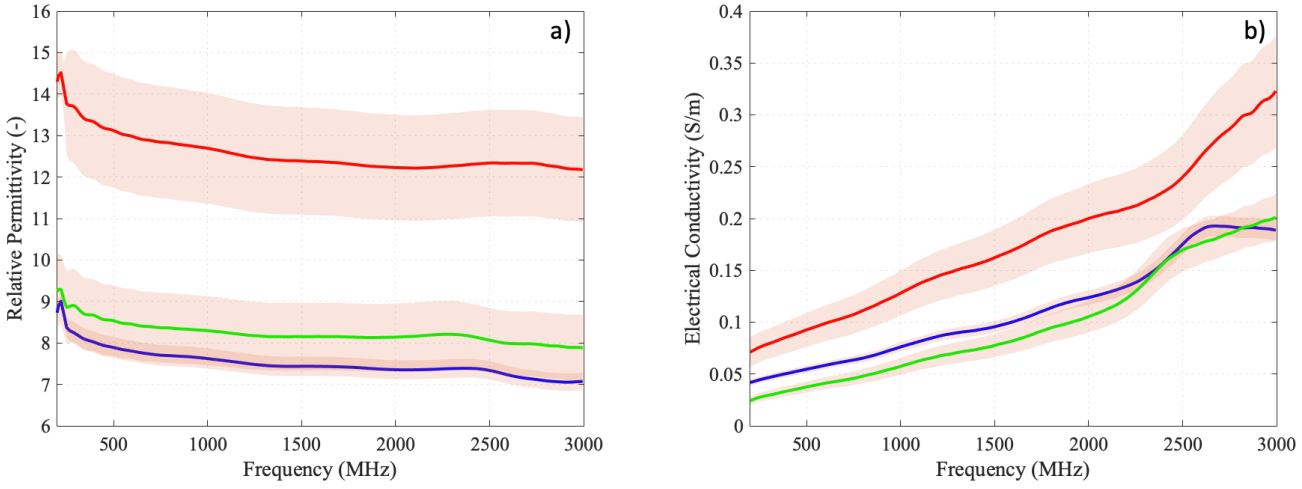


**Figure 3.** Permittivity a) and conductivity b) of the gelatin (red), CNC-gelatin (blue) and DAC-gelatin (green) stabilized emulsions.

*3.2 Rheological and mechanical properties.* Shear rheology was used to determine absolute moduli at T=20 and 45°C, as well as the temperatures at which the gels set and melt. The rheological behavior at T=20°C is important given it is close to typical room temperature, and T=45°C as this is a temperature that a fat phantom should support without loss in mechanical integrity. Figure 4 shows that all emulsions exhibit three phases, one phase where G' is high, which occurs at temperatures close to room temperature or below (green shade in Figure 4), one phase where moduli is reduced rapidly (orange shade, Figure 4) and the third one occurring at T > 40°C (pink shade, Figure 4). The gelatin stabilized emulsion shows a temperature behavior typical for pure gelatin where the gel sets (G' > G") at T = 30°C (arrow 1 in the Figure 4a), followed by a sharp increase in G' until T = 10°C. As the gelatin stabilizing emulsion is reheated, we observe a plateau and sharp reduction in G' at approximately

T = 25°C. The crossover G" > G', defined as the melting temperature, appears at approximately 38°C (arrow 2 in Figure 4a), after which the emulsion is dominated by the viscous component and behaves as a liquid (pink shaded area).

The moduli of the CNC-gelatin (Figure 4b) and the DAC- gelatin (Figure 4c) stabilized emulsions behave similarly upon reduction and increase in temperature. There is no clear setting or melting transition in neither gel, hence absence of arrow 1 and 2 in Figure 4b and 4c. Instead, G' remains at 80 - 100 Pa within the temperature range of 40 to 60°C (red shaded area in Figure 4b and c) and 2000 and 3000 Pa respectively within the temperature range of 10 and 25°C (green shaded area in Figure 4b and c). It is still possible to observe the sharp increase and decrease in the moduli, similar to gelatin stabilized emulsion, with the difference that moduli is not reduced to the same extent at the higher temperatures, and the materials still exhibit G' > G", thus is dominated by the elastic component.

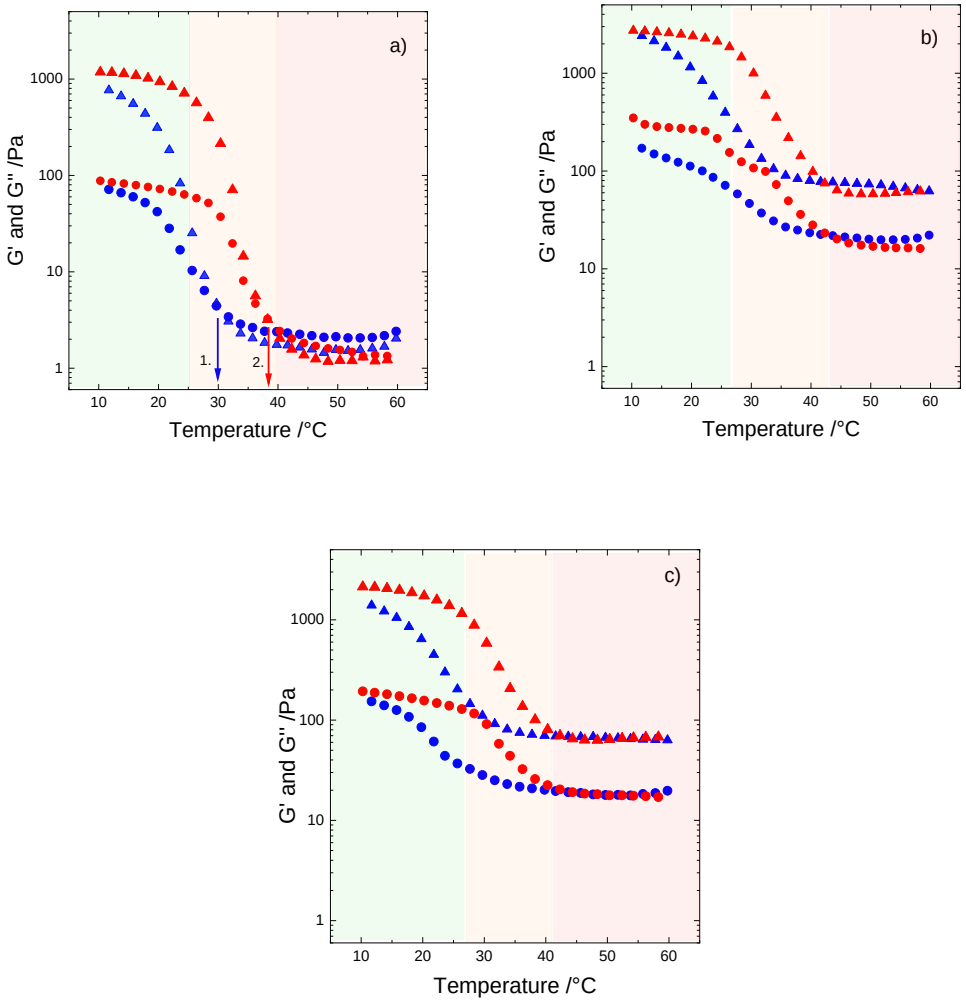


**Figure 4**. G' (triangles) and G" (circles) moduli as a function of temperature for a) gelatin b) CNC-gelatin c) and DAC-gelatin stabilized emulsion. The samples were added at 60°C, followed by cooling (blue symbols) and heating (red symbols). Arrow 1 and 2 points at the setting and melting temperatures of the gel. The measurements were performed at f=1Hz and strain 0.5%.

The force exerted on the fat phantom during use is uniaxial compression. Therefore, stress-strain response of the systems was tested. The stress at break and strain at break are shown in Figure 5. We can see (Figure 5a) that the stress at break for the CNC-gelatin stabilized emulsion is the highest (approx. 57 kPa), followed by gelatin stabilized emulsion (approx. 18 kPa) and DAC-gelatin stabilized emulsion (approx. 10 kPa). The strain at which the gelatin emulsion broke was 75% while CNC broke at 60% and DAC at approx. 58% (Figure 5b).

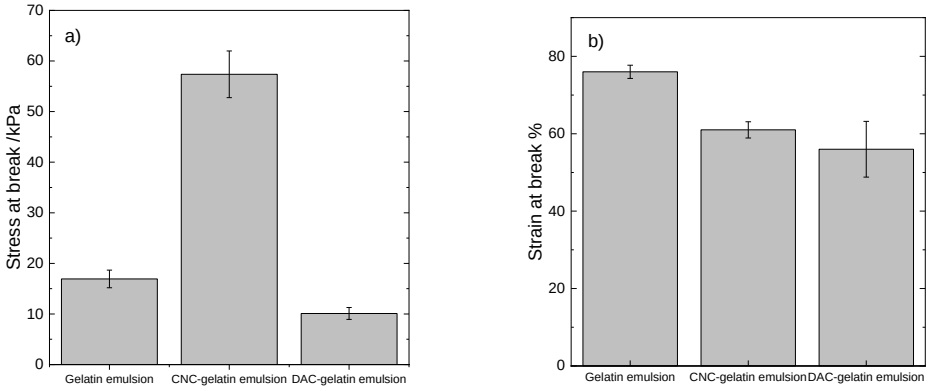


**Figure 5.** Stress at break a) and strain at break b) at room temperature for the gelatin, CNC-gelatin and DAC-gelatin stabilized emulsions.

*3.3 Phantom validation: The compliance with QA guidelines for superficial hyperthermia*. The phantoms were exposed to microwave radiation (60-63 W) from a single antenna for 6 minutes in a set up presented in Figure 1 and temperature was monitored at different locations by thermal sensors. Figure 6a shows the temperature at different locations in horizontal plane, one centimeter below the muscle phantom surface. The antenna was centered above sensor 8 in the probe M3 and temperature rise in the other probes is given with respect to the distance of the probe to the center. The temperature increased nearly 11°C during the 6 minutes test confirming an appropriate function of the antenna and correct execution of the experimental validation.

The temperature at the boundaries between the muscle and fat phantoms and between fat and bolus (Figure 6b) are relevant for the fat phantom verification. The highest temperature of approx. 31°C was measured at the muscle-fat boundary right below the antenna center, with the temperature being approximately 1°C lower, 2 cm from the center (measured at two positions, FM-S1 and FM-S3). The temperature between the bolus and antenna boundary was measured at distance of approximately 1 cm from the central plane due to slight dislocation of the temperature sensor. The temperature between the bolus and antenna reaches a plateau more rapidly than the temperature at the fat-muscle boundary, this is related to the antenna cooling.

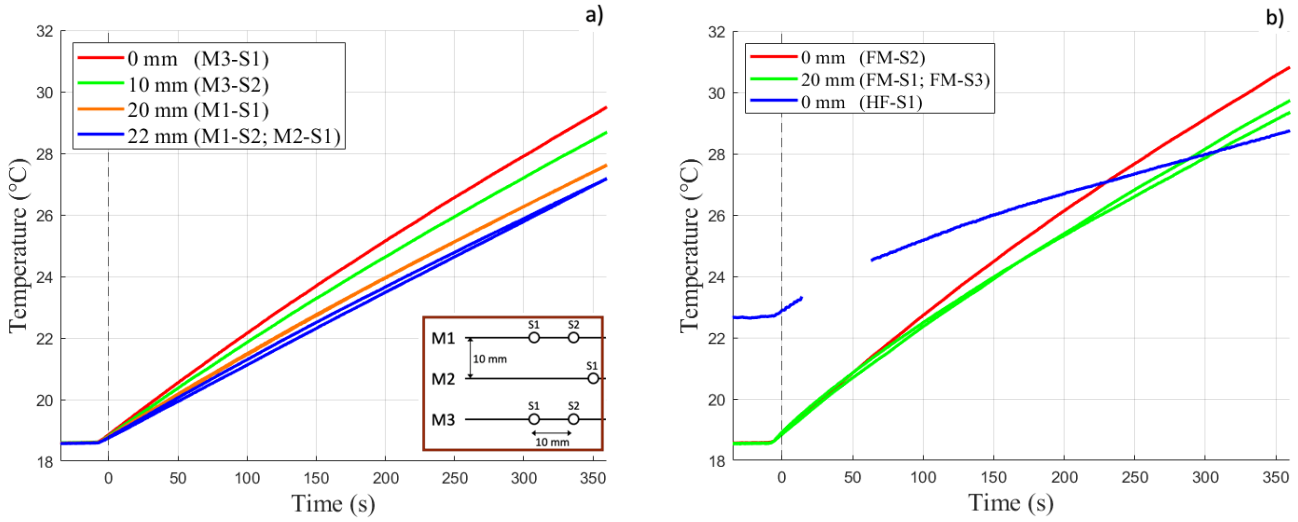


**Figure 6.** Temperatures at different positions a) in the horizontal plane of the muscle phantom and b) at boundaries between muscle/fat and fat/hydrogel bolus (for labelling see Figure 1).

The temperature distributions captured by IR camera immediately after removal of the antenna and hydrogel bolus indicate that the maximal temperatures achieved at the top of the phantom ranges between 34-36°C for gelatin and DAC reinforced phantom while 30°C for the CNC reinforced phantom (Figure 7a-c). The deviation in the heating rates can be attributed to divergence in phantom conductivities. It is apparent that the pure gelatin phantom failed to withstand the stress exerted by the

antenna in combination with temperature increase (Figure 7d). As visible in Figure 7f, the DAC reinforced phantom showed damages at several locations, owing to the physical handling of the phantom.

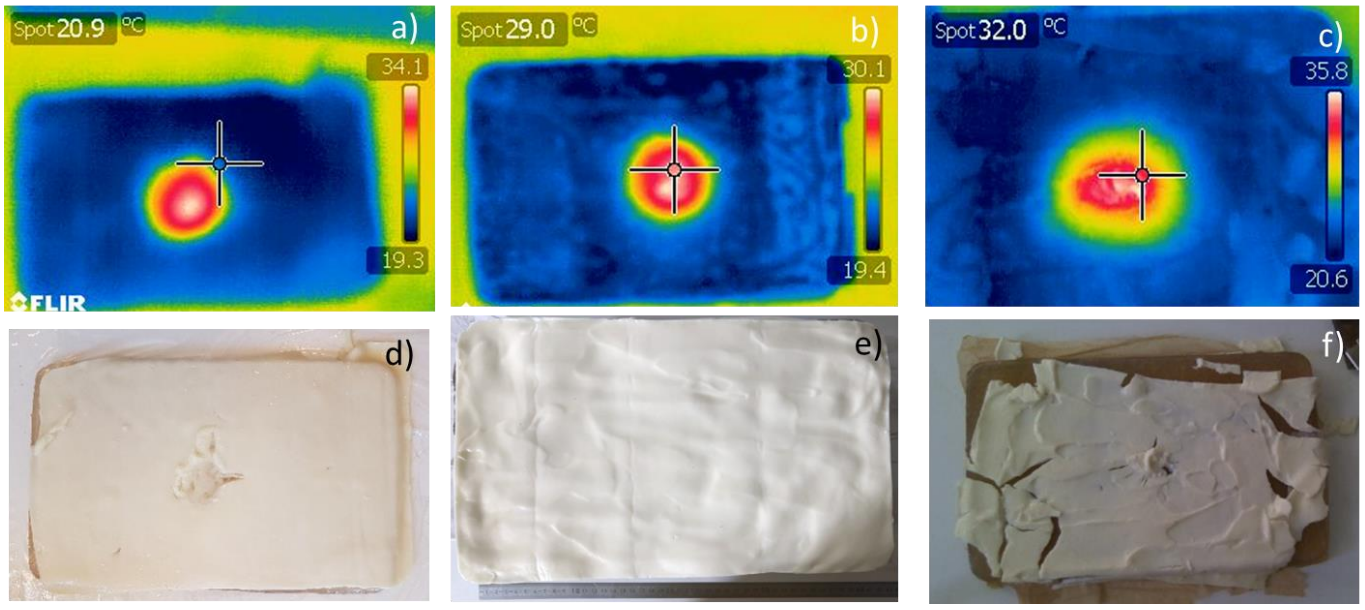


**Figure 7.** Heat distribution of the top layer as captured by IR camera (a, b and c) and visual appearance (d, e and f) after QA validation for superficial hyperthermia of gelatin reinforced fat phantom (a and d), CNC-gelatin reinforced fat phantom (b and e) and DAC-gelatin reinforced fat phantom (c and f).

## 4. Discussion

In this work we hypothesized that the addition of CNCs within the gelatin network could increase its melting temperature, one of the major limitations in use of gelatin reinforced phantoms. Indeed, the influence of temperature on the moduli of the gelatin stabilized emulsion shows distinct sol - gel transition at 28 °C upon cooling and gel to sol upon heating, at 38 °C (Figure 4a). The emulsion stabilized only by gelatin can thus be defined as a liquid at T > 38 °C, making an application as fat phantom according to hyperthermia QA procedures challenging.

While the CNC and DAC stabilized emulsions weaken and the difference between G' and G'' is reduced, at T > 28 °C, the weakening is not to the same extent as the gelatin stabilized emulsion, and importantly they do not exhibit gel-sol transition at 38 °C. The reduced temperature dependence for these systems, can be explained through two different routes. In the case of CNC addition, we believe that we have an electrostatic attraction between the negatively charged CNC and the positively charged gelatin. In the case of addition of DACs in the gelatin matrix, we have an electrostatic attraction like the CNC-gelatin matrix but also a covalent linkage between the aldehyde of the DAC and the amine on the gelatin. Thus, both CNC and DAC addition to gelatin provide increased thermal stability within the investigated temperature range. The results found for DAC gelatin interaction correspond to those reported by Dash *et al.* (2013).

The QA testing of the different emulsions showed clearly that gelatin stabilized emulsion cannot be used as fat phantom, owing to large damages of the phantom under the conditions (power, dielectric properties and time of exposure) used here. The IR image of the gelatin reinforced phantom shows that the temperature reaches those corresponding to those within the area of rapid reduction of gel strength (orange shade Figure 4a). The CNC-gelatin and DAC-gelatin reinforced phantom maintained physical integrity throughout the same heating procedure, confirming the increased thermal stability obtained through the addition of CNC and DAC, in agreement with rheological data.

The surface of the fat phantom is smooth for the gelatin (Figure 7a), while more uneven for the CNC-gelatin and DAC-gelatin reinforced phantoms (Figure 7e and f). This is related to the fact that gelatin behaves as a liquid at the temperatures at which the top layer is prepared, thus easily being poured into the mold. Instead, the CNC-gelatin and DAC-gelatin stabilized emulsions are gel-like (Figure 4 b and c) at similar temperatures thus not filling the mold as efficiently as the gelatin stabilized emulsion.

The stress at break of the DAC-gelatin stabilized emulsion is lower than that of the CNC-gelatin stabilized emulsion (Figure 5), which explains the larger amount of damages shown by the DAC-gelatin reinforced phantom during the QA test (Figure 7f).

Table 2 summarize the different aspects considered during the testing of the three proposed phantoms. The successful QA verification of the CNC-gelatin stabilized emulsion, in combination with the dielectric properties matching those of fat tissues, show its potential for use as fat phantom.

**Table 2:** Consideration of gelatin, CNC-gelatin and DAC-gelatin reinforced phantom suitability for hyperthermia QA procedures. The attributes are rated as achieved (+) or not achieved (-) based on the experimental work in this study.

| | **Gelatin reinforced phantom** | **CNC-gelatin reinforced phantom** | **DAC-gelatin reinforced phantom** |
|---|---|---|---|
| **Commercial availability of ingredients** | + | + | - |
| **Phantom can be prepared at a clinic with a heating plate and high-speed mixing** | + | + | - |
| **Dielectric properties are equivalent to fat tissue** | + | + | + |
| **Thermal stability** | - | + | + |
| **Proof of concept demonstration** | - | + | - |

Subject to further studies are the behavior of the CNC-gelatin reinforced phantom under higher heating rates than used here (2 °C/min), as this may be required in some applications. In addition, the physical networks are subject to relaxations under stress (Schuster *et al.*, 2014) and may yield and reform under pressure. The rearrangement of the physical network may lead to syneresis of oil. Hence, the response of the phantom to prolonged stress could be subject for future studies.

## 5. Conclusion

We have demonstrated that nanocellulose reinforcement increased thermal stability of gelatin hydrogels and can be used to reinforce fat-mimicking phantoms for microwave application. Gelatin, CNC-gelatin and DAC-gelatin reinforced emulsion all fulfill the requirements of phantom dielectric properties. Rheological measurements show that the CNC and DAC addition to the gelatin stabilized emulsion abolish a clear gel-sol transition upon heating. The increased thermal stability of the CNC-gelatin and DAC-gelatin stabilized emulsions was confirmed by the Q, where the gelatin reinforced phantom yielded under the stress and temperature of the antenna. The lower stress at break exhibited by the DAC-gelatin reinforced phantom made it more susceptible to mechanical failure during handling than the other two phantoms.

We have shown that a CNC-gelatin stabilized emulsion further transformed into CNC-gelatin reinforced phantom comply to the requirements for use as fat tissue phantom for microwave diagnostics and hyperthermia treatment.

## Acknowledgments

This work was financially supported by Wallenberg Wood Science Center (WWSC), VinnExcellence center ChaseOn, Barncancerfonden and Kristina Stenborg Stiftelse för Vetenskaplig Forskning. Chalmers Materials Analysis Laboratory is acknowledged for providing access to the CLSM.

## References

Allen S, Kantor G, Bassen H and Ruggera P 1988 Quality-assurance reports: CDRH RF phantom for hyperthermia systems evaluations *Int. J. Hyperthermia* **4** 17-23

Bini M G, Ignesti A, Millanta L, Olmi R, Rubino N and Vanni R 1984 The polyacrylamide as a phantom material for electromagnetic hyperthermia studies *IEEE Trans. Biomed. Eng.* **31** 317-22

Cihoric N, Tsikkinis A, van Rhoon G, Crezee H, Aebersold D M, Bodis S, Beck M, Nadobny J, Budach V, Wust P and Ghadjar P 2015 Hyperthermia-related clinical trials on cancer treatment within the ClinicalTrials.gov registry *Int. J. Hyperthermia* **31** 609-14

Dash R, Foston M and Ragauskas A J 2013 Improving the mechanical and thermal properties of gelatin hydrogels cross-linked by cellulose nanowhiskers *Carbohydr. Polym.* **91** 638-45

Datta N, Ordóñez S G, Gaipl U, Paulides M, Crezee H, Gellermann J, Marder D, Puric E and Bodis S 2015 Local hyperthermia combined with radiotherapy and-/or chemotherapy: Recent advances and promises for the future *Cancer Treat. Rev.* **41** 742-53

Djabourov M and Papon P 1983 Influence of thermal treatments on the structure and stability of gelatin gels *Polymer* **24** 537-42

Dobšíček Trefná H, Schmidt M, Van Rhoon G, Kok H, Gordeyev S, Lamprecht U, Marder D, Nadobny J, Ghadjar P and Abdel-Rahman S 2019 Quality assurance guidelines for interstitial hyperthermia *Int. J. Hyperthermia* **36** 276-93

Duan Q, Duyn J H, Gudino N, de Zwart J A, van Gelderen P, Sodickson D K and Brown R 2014 Characterization of a dielectric phantom for high-field magnetic resonance imaging applications *Med. Phys.* **41** 102303

Dufresne A 2012 *Nanocellulose: From Nature to High Performance Tailored Materials* (Munchen, Germany: Walter de Gruyter)

Eadie L H 2016 Editorial: New technology and potential for telemedicine in battlefield brain injury diagnostics *Concussion* **1**

Fear E C, Bourqui J, Curtis C, Mew D, Docktor B and Romano C 2013 Microwave breast imaging with a monostatic radar-based system: A study of application to patients *IEEE T. Microw. Theory* **61** 2119-28

Fhager A, Candefjord S, Elam M and Persson M 2018 Microwave Diagnostics ahead: Saving time and the lives of trauma and stroke patients *IEEE Microw. Mag.* **19** 78-90

Fontes-Candia C, Lopez-Sanchez P, Strom A, Martinez J C, Salvador A, Sanz T, Trefna H D, Lopez-Rubio A and Martinez-Sanz M 2021 Maximizing the oil content in polysaccharide-based emulsion gels for the development of tissue mimicking phantoms *Carbohydr. Polym.* **256** 117496

Garrett J and Fear E 2014 Stable and Flexible Materials to Mimic the Dielectric Properties of Human Soft Tissues *IEEE Antennas Wirel. Propag. Lett.* **13** 599-602

Hasgall PA, Di Gennaro F, Baumgartner C, Neufeld E, Lloyd B, Gosselin MC, Payne D, Klingenböck A and N K 2018 IT'IS Database for thermal and electromagnetic parameters of biological tissues. ed I Foundation

Hellio D and Djabourov M *Macromol. Symp.,2006),* vol. Series 241*)*: Wiley Online Library) pp 23-7

Issels R D, Lindner L H, Verweij J, Wessalowski R, Reichardt P, Wust P, Ghadjar P, Hohenberger P, Angele M, Salat C, Vujaskovic Z, Daugaard S, Mella O, Mansmann U, Durr H R, Knosel T, Abdel-Rahman S, Schmidt M, Hiddemann W, Jauch K W, Belka C and Gronchi A 2018 Effect of Neoadjuvant Chemotherapy Plus Regional Hyperthermia on Long-term Outcomes Among Patients With Localized High-Risk Soft Tissue Sarcoma: The EORTC 62961-ESHO 95 Randomized Clinical Trial *JAMA Oncol.* **4** 483-92

Ito K, Furuya K, Okano Y and Hamada L 2001 Development and characteristics of a biological tissue-equivalent phantom for microwaves *Electron. Commun. Jpn.* **84** 67-77

Joachimowicz N, Conessa C, Henriksson T and Duchene B 2014 Breast Phantoms for Microwave Imaging *IEEE Antennas Wirel. Propag. Lett.* **13** 1333-6

Kato H, Hiraoka M and Ishida T 1986 An agar phantom for hyperthermia *Med. Phys.* **13** 396-8

Kato H and Ishida T 1987 Development of an agar phantom adaptable for simulation of various tissues in the range 5-40 MHz.(Hyperthermia treatment of cancer) *Phys. Med. Biol.* **32** 221

Kwak H W, Lee H, Park S, Lee M E and Jin H J 2020 Chemical and physical reinforcement of hydrophilic gelatin film with di-aldehyde nanocellulose *Int. J. Biol. Macromol.* **146** 332-42

Lazebnik M, Madsen E L, Frank G R and Hagness S C 2005 Tissue-mimicking phantom materials for narrowband and ultrawideband microwave applications *Phys. Med. Biol.* **50** 4245-58

Madsen E L, Zagzebski J A and Frank G R 1982 Oil-in-gelatin dispersions for use as ultrasonically tissue-mimicking materials *Ultrasound Med. Biol.* **8** 277-87

Markel V A 2016 Introduction to the Maxwell Garnett approximation: tutorial *J. Opt. Soc. Am. A. Opt. Image Sci. Vis.* **33** 1244-56

Meaney P M, Kaufman P A, Muffly L S, Click M, Poplack S P, Wells W A, Schwartz G N, di Florio-Alexander R M, Tosteson T D and Li Z 2013 Microwave imaging for neoadjuvant chemotherapy monitoring: initial clinical experience *Breast Cancer Res.* **15** 1-16

Mondragon G, Peña-Rodriguez C, González A, Eceiza A and Arbelaiz A 2015 Bionanocomposites based on gelatin matrix and nanocellulose *Eur. Polym. J.* **62** 1-9

Nikawa Y, Chino M and Kikuchi K 1996 Soft and dry phantom modeling material using silicone rubber with carbon fiber *IEEE T. Microw. Theory* **44** 1949-53

Parker N G and Povey M J W 2012 Ultrasonic study of the gelation of gelatin: Phase diagram, hysteresis and kinetics *Food Hydrocoll.* **26** 99-107

Paulides M M, Dobsicek Trefna H, Curto S and Rodrigues D B 2020 Recent technological advancements in radiofrequency- andmicrowave-mediated hyperthermia for enhancing drug delivery *Adv. Drug Deliv. Rev.* **163-164** 3-18

Persson M, Fhager A, Trefna H D, Yu Y, McKelvey T, Pegenius G, Karlsson J E and Elam M 2014 Microwave-based stroke diagnosis making global prehospital thrombolytic treatment possible *IEEE Trans. Biomed. Eng.* **61** 2806-17

Poplack S P, Tosteson T D, Wells W A, Pogue B W, Meaney P M, Hartov A, Kogel C A, Soho S K, Gibson J J and Paulsen K D 2007 Electromagnetic breast imaging: results of a pilot study in women with abnormal mammograms *Radiology* **243** 350-9

Porter E, Coates M and Popović M 2015 An early clinical study of time-domain microwave radar for breast health monitoring *IEEE Trans. Biomed. Eng.* **63** 530-9

Rydholm T, Fhager A, Persson M and Meaney P M 2017 A first evaluation of the realistic Supelec-breast phantom *IEEE J. Electromagn., RF, Microw. Med. Biol.* **1** 59-65

Schuster E, Eckardt J, Hermansson A M, Larsson A, Loren N, Altskar A and Strom A 2014 Microstructural, mechanical and mass transport properties of isotropic and capillary alginate gels *Soft Matter* **10** 357-66

Sihvola A H 1999 *Electromagnetic mixing formulas and applications* (London, UK: The Institution of Electrical Engineers)

Simon A, Grohens Y, Vandanjon L, Bourseau P, Balnois E and Levesque G 2003 A comparative study of the rheological and structural properties of gelatin gels of mammalian and fish origins *Macromol. Symp.* **203** 331-8

Simpkin R 2010 Derivation of Lichtenecker's Logarithmic Mixture Formula From Maxwell's Equations *IEEE T. Microw. Theory* **58** 545-50

Takook P, Persson M, Gellermann J and Trefna H D 2017 Compact self-grounded Bow-Tie antenna design for an UWB phased-array hyperthermia applicator *Int. J. Hyperthermia* **33** 387-400

Tosh S M and Marangoni A G 2004 Determination of the maximum gelation temperature in gelatin gels *Appl. Phys. Lett.* **84** 4242-4

Trefná H D, Crezee J, Schmidt M, Marder D, Lamprecht U, Ehmann M, Nadobny J, Hartmann J, Lomax N and Abdel-Rahman S 2017 Quality assurance guidelines for superficial hyperthermia clinical trials II. Technical requirements for heating devices *Strahlenther. Onkol.* **193** 351-66

Trefna H D and Ström A 2019 Hydrogels as a water bolus during hyperthermia treatment *Phys. Med. Biol.* **64** 115025

van Vlierberghe S, Dubruel P and Schacht E 2011 Biopolymer-based hydrogels as scaffolds for tissue engineering applications: a review *Biomacromolecules* **12** 1387-408

Wang W, Zhang X, Teng A and Liu A 2017 Mechanical reinforcement of gelatin hydrogel with nanofiber cellulose as a function of percolation concentration *Int. J. Biol. Macromol.* **103** 226-33

Yuan Y, Wyatt C, Maccarini P, Stauffer P, Craciunescu O, MacFall J, Dewhirst M and Das S K 2012 A heterogeneous human tissue mimicking phantom for RF heating and MRI thermal monitoring verification *Phys. Med. Biol.* **57** 2021-37